Tectonics

RESEARCH ARTICLE
10.1029/2020TC006479

Paleoseismic Evidence of an M_w 7 Pre-Hispanic Earthquake in the Peruvian Forearc

Carlos Benavente[1], Sam Wimpenny[2], Lorena Rosell[1], Xavier Robert[3], Anderson Palomino[1], Laurence Audin[3], Enoch Aguirre[1], and Briant García[1]

[1]Instituto Geológico, Minero y Metalúrgico INGEMMET, San Borja, Perú, [2]Department of Earth Sciences, COMET, Bullard Laboratories, University of Cambridge, Cambridge, UK, [3]Université Grenoble Alpes, CNRS, IRD, ISTerre, Grenoble, France

Key Points:

- We describe a ~100-km long, 2–4-m high segmented fault scarp in the forearc of southern Peru along the Incapuquio Fault System
- We argue that the scarps were formed during an M_w 7.4–7.8 earthquake that ruptured the Incapuquio Fault in the early 15th century
- The kinematics of the Incapuquio Fault suggest that it breaks following strain accumulation in the forearc during the interseismic period of the megathrust earthquake cycle

Supporting Information:

Supporting Information may be found in the online version of this article.

Correspondence to:

C. Benavente,
cbenavente@ingemmet.gob.pe

Citation:

Benavente, C., Wimpenny, S., Rosell, L., Robert, X., Palomino, A., Audin, L., et al. (2021). Paleoseismic evidence of an M_w 7 pre-Hispanic earthquake in the Peruvian forearc. *Tectonics*, *40*, e2020TC006479. https://doi.org/10.1029/2020TC006479

Received 11 AUG 2020
Accepted 10 MAY 2021

Abstract We present the results of a paleoseismic survey of the Incapuquio Fault System, a prominent transpressional fault system cutting the forearc of South Perú. High-resolution Digital Elevation Models, optical satellite imagery, radiocarbon dating, and paleoseismic trenching indicate that at least 2–3 m of net slip occurred on the Incapuquio Fault generating a complex, ~100-km long set of segmented fault scarps in the early 15th century (~1400–1440 CE). We interpret the consistent along-strike pattern of fault scarp heights, geometries and kinematics to reflect a surface rupture generated by a single M_w 7.4–7.7 earthquake, suggesting that brittle failure of the forearc poses a significant, yet mostly overlooked, seismic hazard to the communities in coastal areas of Perú. The timing of this earthquake coincides with the collapse of the Chiribaya civilization in ~1360–1400 CE, and we present evidence of damaged buildings along the fault trace that may be of Chiribayas age. Our surface faulting observations, when combined with observations of deformation in the forearc from geodesy and seismology, also demonstrate that the forearc in South Perú experiences a complex, time-varying pattern of permanent strain, with evidence for trench-parallel shortening, trench-parallel extension, and trench-perpendicular shortening all in close proximity but in different periods of the megathrust earthquake cycle. The kinematics of recent slip on the Incapuquio Fault are consistent with the sense of interseismic strain within the forearc measured by GPS, suggesting the fault is loaded toward failure between megathrust earthquakes.

1. Introduction

The major seismic hazard along the coast in South Perú is widely attributed to the M_w 8–9 earthquakes that occur every 150–300 years due to strain accumulation and release on the interface between the subducting Nazca plate and the overriding South American plate (Villegas-Lanza et al., 2016). The possibility of large earthquakes generated by faults rupturing the forearc is generally overlooked. For example, mechanical models of the subduction zone typically treat the forearc as being purely elastic over the hundred-year megathrust earthquake cycle (Villegas-Lanza et al., 2016), while over million-year time scales permanent deformation within the South American plate is assumed to occur solely in the sub-Andean fold-thrust belts in the back-arc (Norton & Schlunegger, 2011). However, there is growing geomorphological evidence for Quaternary faulting within the forearc of South Perú (Audin et al., 2006; Benavente et al., 2017; Macharé et al., 2003) and northern Chile (Allmendinger et al., 2005; Binnie et al., 2020; Loveless et al., 2010). Major earthquakes within the forearc may occur by linking a complex series of oblique faults during a single rupture (e.g., Hamling et al., 2017; Schermer et al., 2020), which could pose a significant, yet poorly constrained, seismic hazard in the region. Similarly, there is tentative evidence that slip on forearc faults may change the stress state on highly strained sections of the megathrust, triggering large megathrust earthquakes (González et al., 2015). Therefore, understanding the magnitude, kinematics, and history of fault slip in the forearc is key to assessing the mechanics and the seismic hazard within subduction zones.

In this study, we investigate the timing and size of a past surface-rupturing earthquake in the forearc of South Perú, which generated fault scarps along the southern segment of the Incapuquio Fault System (herein referred to as the IFS) between Moquegua and Aguas Calientes (e.g., Jacay et al., 2002; Wilson & García, 1962) (Figure 1). Microseismicity studies have previously suggested part of the IFS may be active (David et al., 2005). However, no major historical or instrumental earthquakes have been reported along the structure (e.g., Devlin et al., 2012; Dorbath et al., 1990). We argue that the southern segment of the IFS

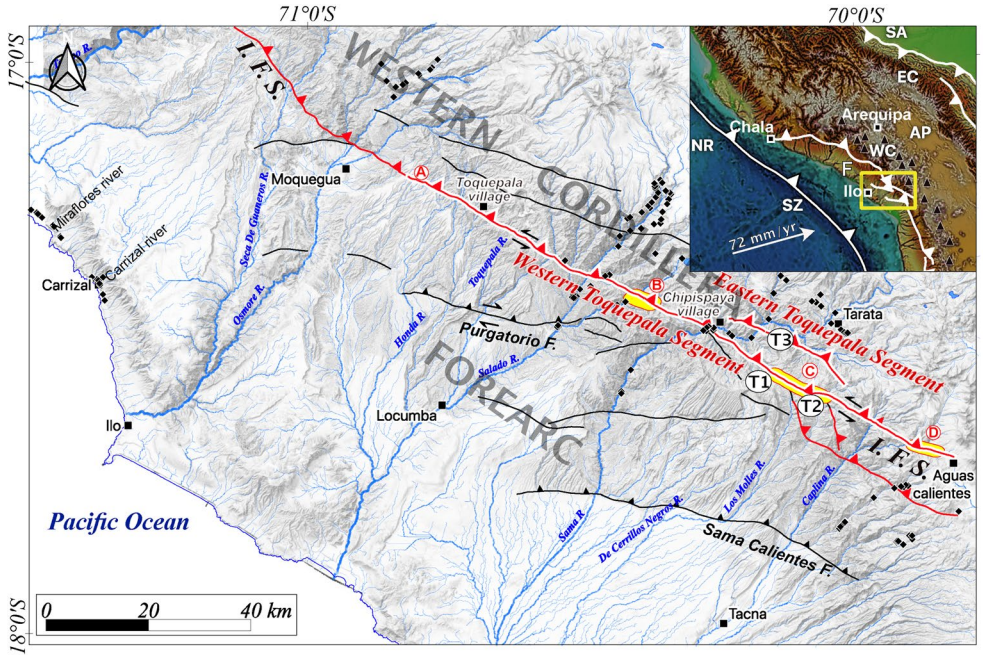

Figure 1. Overview map of the Incapuquio Fault System (IFS). The red line with white borders represents the section of the IFS where we identified recent surface ruptures. Black lines are mapped active faults in the region (Audin et al., 2006; Benavente et al., 2017). The letters A, B, C, and D indicate the location of the Toquepala, Chintari, Tauja, and Santa Elena zones, respectively. The yellow zones indicate the areas where we built high-resolution DEMs using a drone. T1, T2, and T3 mark the locations of paleoseismological trenches. Blue lines represent the major rivers, squares indicate the main population centers and the black diamonds represent archeological sites (https://www.geoidep.gob.pe/ministerio-de-cultura). The inset shows the location of the study area in a yellow rectangle with the main morphological units of the Andes labeled (F, Forearc; WC, Western Cordillera; AP, Altiplano; EC, Eastern Cordillera; SA, Sub-Andes; NR: Nazca Ridge). Plate velocities are shown relative to stable South American (DeMets et al., 2010) and black triangles mark active volcanoes.

ruptured in at least one earthquake that could have been up to M_w 7.4–7.7 from observations of fault scarps in optical satellite imagery, high-resolution Digital Elevation Models (DEMs), field mapping, slickenline measurements, paleoseismic trenching, and radiocarbon dating. We discuss how the kinematics of this earthquake compares to other kinematic indicators of deformation in the forearc of South Perù. Finally, we present evidence that a large earthquake on the IFS may have contributed to the collapse of the Chiribaya civilization at the start of the 15th century.

2. Geological and Seismotectonic Setting

The Andes are the classic example of mountain building along a convergent ocean-continent plate boundary. Crustal thickening and uplift along the western margin of South America has been driven by Mesozoic-Cenozoic subduction of the Nazca Plate (Horton et al., 2001; Isacks, 1988; Jaillard et al., 2002; McQuarrie et al., 2005; Ramos, 2010). At the latitude of South Perú, the Central Andes can be divided into five different zones based on their morphology: (a) the forearc, (b) the Western Cordillera, (c) the Altiplano, (d) the Eastern Cordillera, and (e) the sub-Andes (Figure 1, inset). The forearc morphology is characterized by a gentle, westward-dipping topographic slope extending from the magmatic arc toward the coastline. Ephemeral rivers draining across the forearc from the Western Cordillera have incised deep, NE-SW trending valleys into its gentle surface, creating a prominent erosional fabric and depositing vast Quaternary alluvial fans (Figure 1). Faulting within the forearc generates differential uplift, causing variations in the depth of incision within these valleys, abandonment of the alluvial fan surfaces, and deflections in the NE-SW drainage pattern (Audin et al., 2006; Hall et al., 2012). Thermochronological dating of exhumation within canyons near Arequipa suggests a period of enhanced incision in the Western Cordillera and forearc initiated around 14-10 Ma and ended 5-2.2 Ma (Schildgen et al., 2007), around the same time as paleoelevation estimates

imply significant uplift of the Western Cordillera (Garzione et al., 2017). Since 5-2.2 Ma, drainage has been focused into the canyon systems, and the extreme aridity has led to low denudation rates (<0.5 m/Ma) on the abandoned alluvial fan surfaces (e.g., Dunai et al., 2005; Hall et al., 2012). Therefore, fault-related Quaternary geomorphology is well preserved throughout the forearc.

The role that forearc faults play in uplifting the Western Cordillera relative to the coastline and in accommodating oblique subduction within South Perú remains unclear. Benavente et al. (2017) identified several NW-SE and E-W trending, active left-lateral transpressional faults in the forearc of South Perú that uplift the Western Cordillera and accommodate a component of the oblique convergence (Figure 1). In contrast, Schildgen et al. (2009) proposed from field observations and thermochronology studies that between 14 and 2 Ma normal faulting in the forearc generated up to 2 km of relief in the Arequipa region. Norton and Schlunegger (2011) have argued from landscape modeling of channel morphologies that little deformation has occurred in the Perúvian forearc since ~7 Ma. While, Hall et al. (2012) and Armijo et al. (2015) have proposed that recent deformation of the Western Cordillera and forearc is associated with monoclinal warping above west-vergent thrusts subparallel to the subduction megathrust. Differentiating between these contrasting structural interpretations of deformation in the forearc requires measurements of the geometry and kinematics of faults in the region.

The IFS is one of the major faults within the forearc of South Perú and trends subparallel to the topographic transition between the forearc coastal plain and the deeply incised Western Cordillera (Figure 1). The IFS consists of multiple fault strands active during the Cenozoic that cut Jurassic sedimentary and late Cenozoic volcaniclastic rocks with transpressional kinematics, and which dip steeply toward the northeast beneath the Western Cordillera (Bellido, 1979; Jacay et al., 2002; Wilson & García, 1962). The earliest studies to map the IFS also identified near-vertical bedrock scarps, and fresh scarps in alluvial deposits, along the fault trace with an apparent normal sense of motion (Audin et al., 2006; Macharé et al., 2003; Sébrier et al., 1985). The reported scarps have an along-strike length of almost 100 km and may represent the surface rupture generated in a significant pre-historic earthquake; though no paleoseismic trenching, dating, or detailed scarp morphology data currently exist to test this hypothesis. In addition, several of the newly identified active transpressional fault systems in the forearc connect with the IFS (Benavente et al., 2017; Hall et al., 2012), raising the question of whether recent slip on the IFS was in fact normal in sense. In this study, we explore the recent kinematics and history of slip on the IFS using structural and geomorphological measurements of these fault scarps.

3. Methods

3.1. Fault Scarp Mapping

The Geological Survey of Perú (INGEMMET) has been updating the national neotectonic map (e.g., Benavente et al., 2013, 2018; Macharé Ordoñez et al., 2009). As part of this project, we mapped the IFS fault scarps using 1-m resolution optical satellite imagery from Digital Globe (Google Earth) and 12-m resolution Tandem-X DEMs (Rizzoli et al., 2017), covering a surface area of ~2,000 km^2 with detailed inspection. Within the optical satellite data, the IFS is delineated by a sharp, linear boundary caused by vegetation contrasts, contrasts in bedrock color, shading from topographic scarps, deflections in the drainage pattern, and topographic steps. From these satellite observations, we built a preliminary map of the 100 km long fault trace between Moquegua and Aguas Calientes. These preliminary fault maps were then used to guide subsequent field work.

In order to study the morphology of the fault scarps, we constructed high-resolution DEMs at three localities (sites B, C, and D in Figure 1) using the structure-from-motion technique. Photographs were collected from an eBee senseFly drone and processed with Agisoft Photoscan (Westoby et al., 2012). Ground control points used to guide the image matching were located using differential GPS. The resulting point clouds have at least 1 point per 10 cm^2 horizontal resolution, and are complemented with orthomosaic imagery at 5 cm^2 pixel resolution. The DEMs are available through OpenTopography (www.opentopography.org; see Acknowledgments).

Fault scarp heights were calculated using two methods: (a) estimating the vertical separation of correlatable surfaces either side of a scarp using two-dimensional topographic profiles perpendicular to the scarp strike

(e.g., Wolfe et al., 2019), or (b) estimating vertical offsets from offset layers exposed in trench sections (e.g., Morell et al., 2018). Uncertainties in the scarp heights due to noise in the point cloud and the extrapolation of the alluvial surfaces across the scarp were typically an order of magnitude smaller (~10–20 cm) than the along-strike deviations in the measured scarp heights. The scarp heights were converted into fault throw and net fault slip using the strike, dip, and rake measurements of slickenlines exposed on nearby bedrock sections of the fault plane, and the dip and aspect of the offset surfaces (e.g., Mackenzie & Elliott, 2017). Where multiple scarp heights could be measured on a single section of the fault, we used the distribution of scarp heights and differences in the scarp morphology to discriminate cumulative scarps from single-event scarps (e.g., Grützner et al., 2017).

3.2. Fault Kinematics

Many of the fault scarps along the IFS formed in consolidated alluvial and volcaniclastic rocks and preserved slickenlines on an exposed surface, typically a southwest-facing overhang. From herein, we refer to these types of scarps as "bedrock scarps." Given the protracted Cenozoic history of movement along the IFS, it is possible that sections of the bedrock scarps preserve slickenlines from ancient episodes of slip that do not reflect the fault's current kinematics. Therefore, we only collected slickenline measurements from bedrock scarps that either show evidence for offsetting late Quaternary sediments, or transition along-strike into a scarp that offsets late Quaternary deposits.

3.3. Paleoseismology

In order to determine the chronology of scarp formation, we studied the stratigraphy in three natural exposures of the fault using the standard protocol for cleaning, recording, and analysis proposed by McCalpin (2009). Charcoal, sediment, and root samples from offset layers and colluvial wedges were collected for radiocarbon dating. Each of the samples was placed in an aluminum foil packet, and was dated by the Beta Analytic laboratory in Miami. All radiocarbon ages were modeled with the OxCal v4.3.2 online program, which uses a Bayesian statistical method (Bronk Ramsey, 2017) to propagate analytical errors and errors in the calibration curve SHCal13 (Hogg et al., 2013) through the age calculation, providing probabilistic estimates for the age of each sample.

3.4. Teleseismic Body-Waveform Modeling

The focal mechanisms of earthquakes can place additional constraints on the timing and kinematics of deformation in the forearc around the IFS. We used the long-period teleseismic body-waveform modeling program MT5 of Zwick et al. (1994), which is based on the algorithm of McCaffrey and Abers (1988), to determine point-source focal mechanisms and centroid depths for two moderate-magnitude earthquakes with epicenters near the IFS (Event 1: M_w 5.7 August 26, 2003 and Event 2: M_w 5.5 November 20, 2006) and one earthquake that ruptured the forearc to the southwest of the IFS 20 km offshore (Event 3: M_w 6.2 May 06, 2010). The MT5 waveform-modeling method has been described extensively elsewhere (e.g., Devlin et al., 2012; Molnar & Lyon-Caent, 1989); therefore, we provide the details of the data processing, and the velocity models used to generate the synthetic seismograms, in Text S1.

4. Results

4.1. Fault Scarps Along the Incapuquio Fault Zone

Fault scarps on the IFS can be traced discontinuously between Moquegua and Aguas Calientes using optical satellite imagery and high-resolution DEMs (Figure 1). The scarps can't be traced continuously, because rivers cross cutting the fault have incised deep and wide canyons, eroding the morphological evidence of the IFS in several areas. As a result, the morphological trace of the fault is partitioned into four different along-strike zones: The Toquepala, Chintari, Tauja, and Santa Elena Zones, which are labeled A, B, C, and D in Figure 1, respectively.

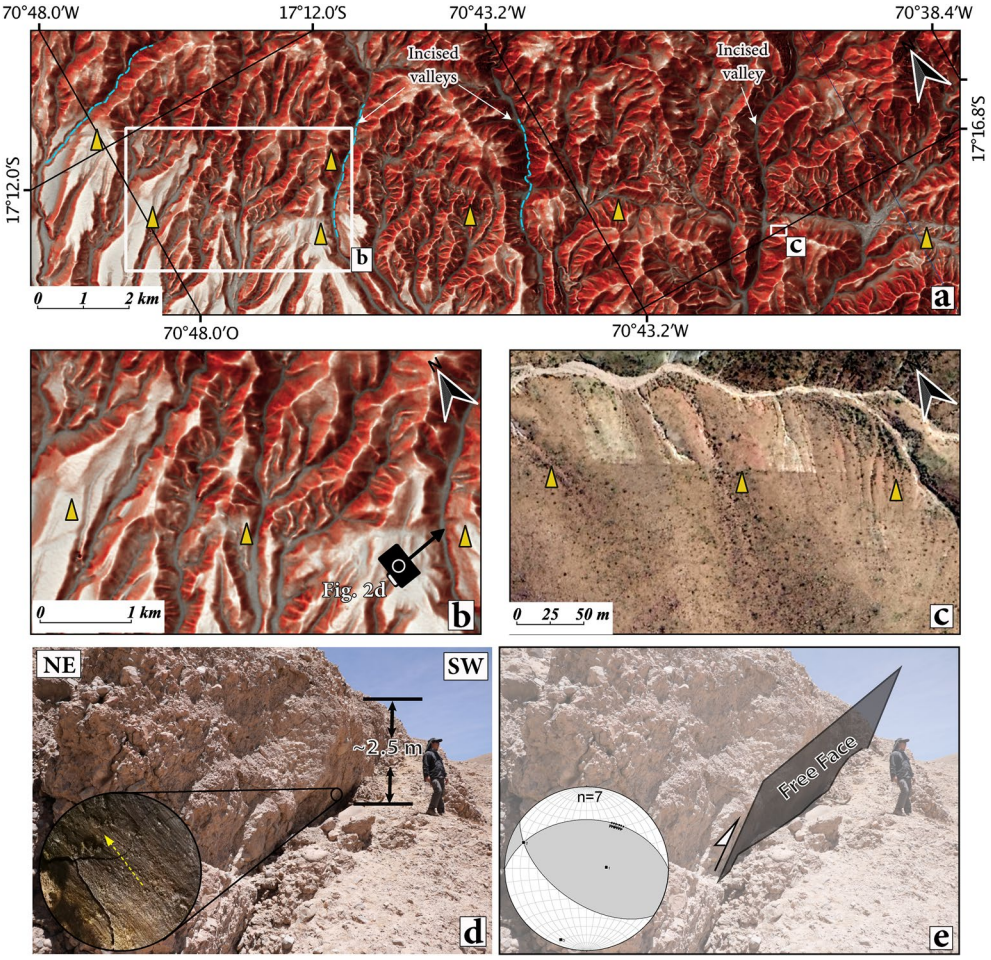

Figure 2. Toquepala Zone. (a) Topography from a 12 m Tandem-X DEM colored as a Red Relief Image Map (Chiba et al., 2007) highlighting the surface scarps. Yellow arrows locate the trace of the fault. The white rectangles indicate the location of Figures 2b and 2c. (b) Zoom-in on the northern end of the fault trace. The streams that drain through the elevated surface in the hanging-wall of the IFS have excavated narrow valleys. The camera symbol indicates the direction of the photos presented in Figures 2d and 2e. (c) Digital Globe satellite image (from Google Earth) of the fault scarp. In this area, the fault scarp is picked out by a sharp change in stream incision across the fault and the vegetation. (d) Bedrock scarp with a free face of ~2.5 m, with a close-up photo of subvertical slickenlines inset. (e) Sketch interpretation of Figure 2d, and a stereonet showing fault slickenline data (black arrows indicating movement of hanging-wall with respect to the footwall) produced using FaultKinWin(R) program (Allmendinger, 2018). IFS, Incapuquio Fault System.

4.1.1. Toquepala Zone

The Toquepala Zone is the northern-most section of the IFS where we have been able to identify fresh fault scarps (A in Figure 1). In this region, the IFS is marked by a 20 km long, NW-SE trending topographic step in the west-dipping slope between Toquepala Village and the Rio Salado, with the fault trace being picked out by sharp changes in stream incision and rerouted drainage along the fault strike (Figures 2a and 2b). The fault is also distinct in geological maps of the region, as it separates late Cretaceous-early Paleogene granite porphyrys that outcrop northeast of the fault from Eocene-Miocene volcaniclastic rocks to the southwest (INGEMMET, 2017). The fault trace itself has a number of left steps, where the fault strike becomes oriented ~E-W (Figure 2a). We mapped 8 km of fault scarps at Toquepala that were delineated by changes in the vegetation, shading or ground surface color in optical satellite images (Figure 2c). In between the fault scarps, rivers and mass movements have eroded morphological evidence of recent faulting.

During the field investigation, we identified a locally exposed, ~2.5 m high bedrock scarp within a 1 km left step in the fault trace (Figures 2d and 2e). The scarp cuts through consolidated, poorly sorted debris

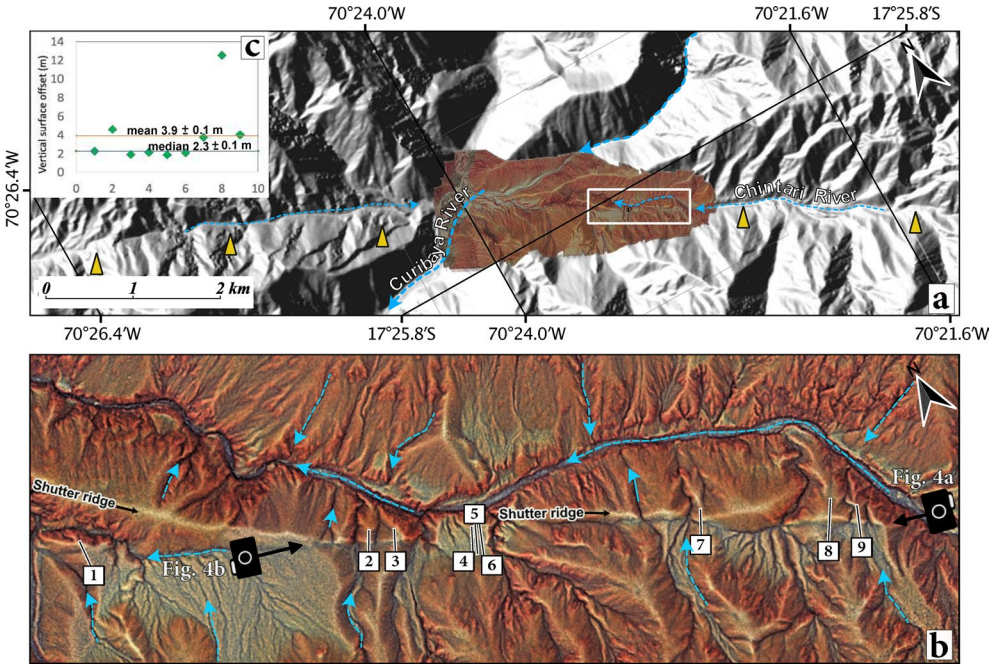

Figure 3. Chintari Zone. (a) Background topography from a 12 m Tandem-X DEM, with light blue dashed arrows indicate the main streams. Overlain is a 10-cm high-resolution DEM colored as a Red Relief Image Map. The white rectangle indicates the location of Figure 3b and the yellow triangles mark the fault trace. (b) Zoom-in of the Red Relief Image Map showing the scarp morphologies. Black lines perpendicular the scarps indicate the locations of topography profiles. The black arrows point to shutter ridges. All topography profiles are numbered and shown in supporting information. The camera symbols indicate the direction of the photos presented in Figures 4a and 4b. (c) Vertical scarp heights measured from the eight fault-perpendicular profiles extracted from the high-resolution DEM shown in (b). The uncertainty of each measurement is ~10 cm, therefore is smaller than the symbol (see Table S1). The mean (orange line) and median (blue line) of all measurements are also shown.

flow deposits containing subangular to rounded clasts ranging in size from pebbles to boulders. Fault plane measurements from the exposed scarp had a consistent orientation 270°/40°. Slickenlines preserved on the surfaces of the clasts within the debris flow deposit also had a relatively consistent orientation, pitching between 58° and 67° toward the northeast (Figure 2d, inset). The slickenline orientations suggest the IFS accommodates left-lateral transpression near its northern tip (Figure 2e, inset).

4.1.2. Chintari Zone

The Chintari Zone stretches for ~20 km along an NW-SE trend between the Rio Salado and Rio Sama (B in Figure 1). The fault trace is poorly exposed in this zone due to extensive incision from southwest draining rivers. However, fault scarps that follow the projected trace of the IFS are occasionally found within the upper reaches of tributaries. We mapped 6 km of continuous scarps cutting alluvial gravels and late Cretaceous-Paleogene volcaniclastic rocks (INGEMMET, 2017) that run along the southern margin of the Chintari river valley (Figure 3a). In many places, northward draining streams run parallel to shutter ridges, incising the fault footwall as drainage becomes rerouted along the fault, accentuating the topographic expression of the scarps (Figure 3b).

We extracted nine topographic profiles perpendicular to the fault from a high-resolution DEM of the lower 2 km of the Chintari river valley (Figure 3a). The profile locations are shown in Figure 3b and the distribution of vertical scarp heights calculated from these profiles are shown in Figure 3c. The raw topographic profiles are shown in Supporting Information. Within the Chintari zone, the scarp heights vary between 1.9 ± 0.1 and 12.5 ± 0.1 m, with a mean height of 3.9 ± 0.1 m and a median height of 2.3 ± 0.1 m. A single scarp of 12.5 m (profile 8) is a clear outlier, and corresponds to the scarp shown in the background of Figure 4a that has been deeply eroded within its footwall by a stream that drains along its strike.

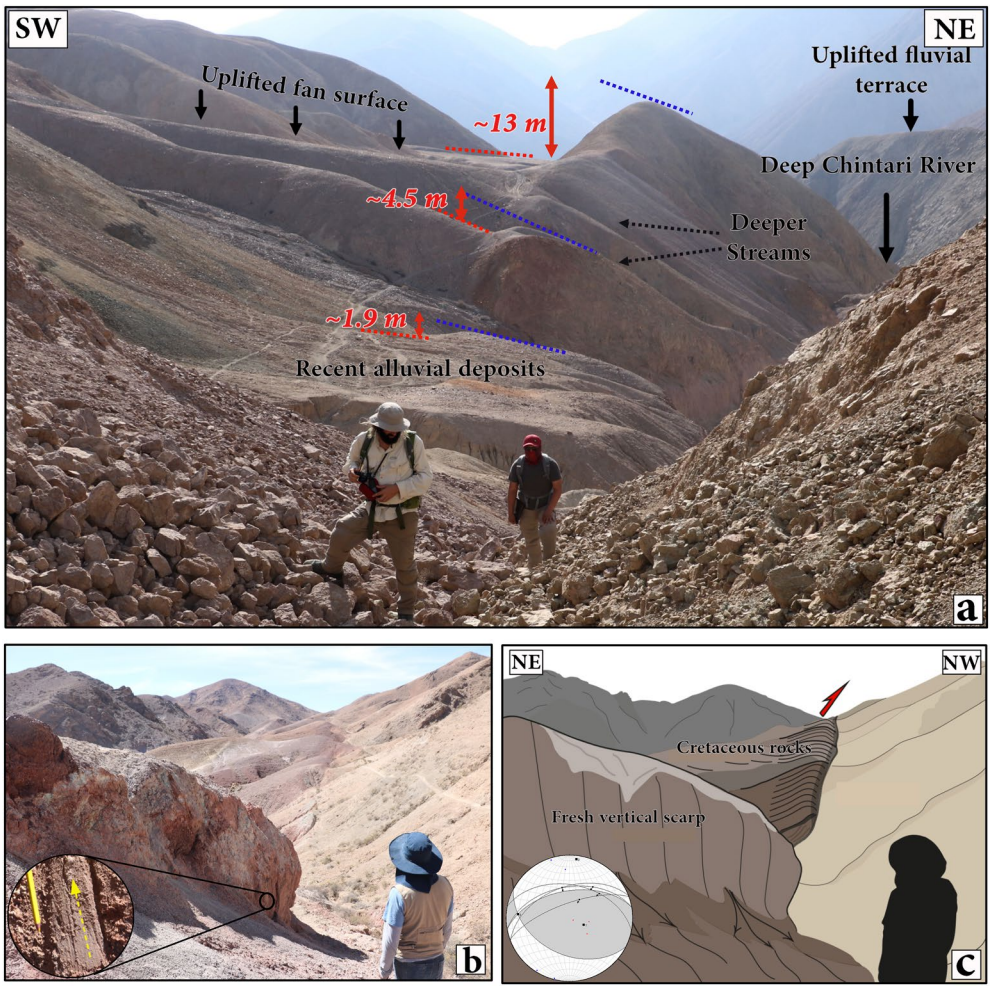

Figure 4. Photographs of fault scarps in the Chintari Zone. (a) Photograph of the cumulative scarp near profiles 8 and 2 (see Figure 3b). In the area of the active alluvial fan in the foreground, only the last scarp-forming event (~1.9 m) has been preserved. In the background, the cumulative scarps can clearly be seen. (b) Fresh, vertical bedrock scarp of up to ~2-m high with a free face (see location in Figure 3b) where we were able to measure slickenlines. A close-up photo is shown inset of the slickenlines is shown inset. (c) Sketch interpretation of Figure 4b, and a stereonet showing faults the fault slickenline data (black arrows indicating movement of hanging-wall with respect to the footwall).

Near the confluence between the Rio Curibaya and the Rio Chintari, we identified a section of ~2 m high fault scarps cutting consolidated, poorly sorted alluvial gravels with pebble to boulder-sized clasts. The fault plane had a highly variable orientation of 249°–281°/46°–71° with the slickenlines pitching between 55° and 85° toward the north or northeast, suggesting the scarps were formed due to reverse slip with a significant left-lateral component. The variability in the fault plane measurements resulted from the irregular shape of the fault plane in the coarse alluvial deposits. Further along-strike, late Cretaceous volcaniclastic rocks to the northeast of the fault trace have been thrusted over the young alluvial gravels (Figures 4b and 4c), confirming that the IFS has recently accommodated transpression with a left-lateral component of slip in the Chintari zone.

4.1.3. Tauja Zone

The Tauja Zone lies southeast of Chintari and spans a 30 km section of the IFS between the Rio Sama and the Rio Caplina (C in Figure 1). The fault trace in this region splits into two subparallel strands—a northern and southern strand (Figure 1). The southern strand consists of 15 km of prominent, linear fault scarps that are associated with deflected river networks (Figures 5a–5d), beheaded streams, and shutter ridges (Figures 5b–5d). The scarps mark the displacement of dark-gray Paleozoic volcaniclastic rocks and lower

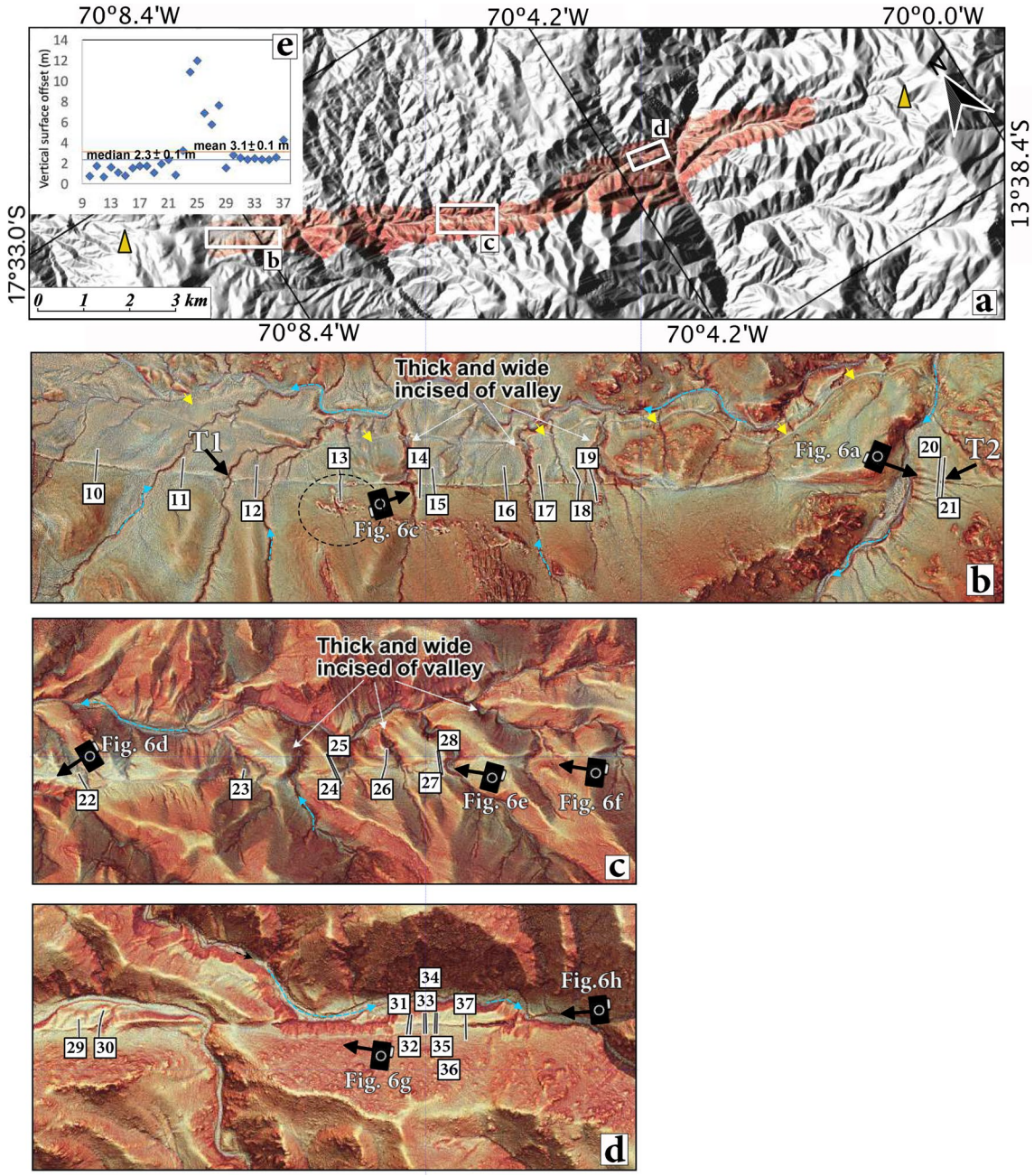

Figure 5. Tauja Zone. (a) Background topography from a 12 m Tandem-X DEM overlain with a Red Relief Image Map of the high-resolution DEM. The white rectangles indicate the location of Figures 5b–5d and yellow triangles show the fault trace. (b–d) Red Relief Image Maps derived from the 10-cm resolution DEM showing the scarp morphology. In (b) yellow arrows indicate an old, single-track road that skirts the Western Cordillera from north to south and links small buildings and irrigation canals. The black-dashed circle highlights buildings that could correspond to the Chiribaya period, based on the type and ceramics found. As with previous figures, the light blue arrows indicate the direction of streamflow and the black bars indicate the extracted topography profiles with corresponding numbering. The camera symbols indicate the direction of the photos shown in Figure 6. (e) Scarp heights measured from the 28 fault-perpendicular profiles taken across the high-resolution DEM, with mean and median highlighted. DEM, Digital Elevation Models.

Cretaceous andesitic lava flows that outcrop northeast of the fault trace over light-brown alluvial gravels to the southwest of the fault trace (Figures 6a–6d). Geological maps of the region suggest that the alluvial gravels to the southwest of the fault scarps are Holocene in age, and sit unconformably on Paleozoic volcaniclastic rocks in the western section of the Tauja Zone (INGEMMET, 2017) (Figures 6a and 6b). In the eastern section of the Tauja Zone, the Holocene alluvial gravels sit unconformably above an inlier of Mesozoic rocks

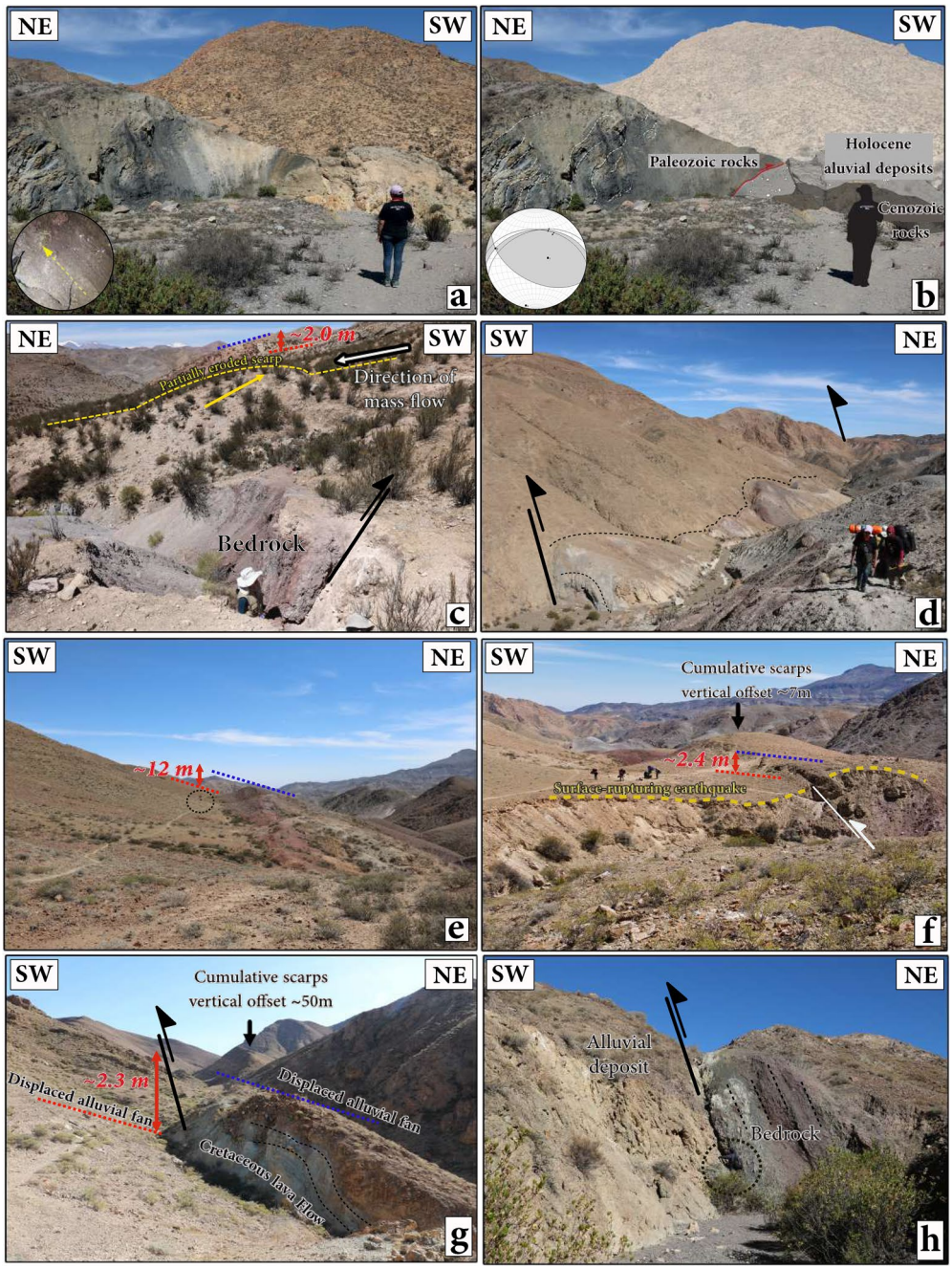

Figure 6. Photographs of fault scarps in the Tauja Zone. (a) Photo showing the fault juxtaposing dark Paleozoic volcaniclastic rocks against lighter Holocene alluvial gravels, with a close-up photo of subvertical slickenlines shown inset. (b) Interpretation of Figure 6a, plus a stereonet showing fault slickenline data (black arrows indicating movement of hanging-wall with respect to the footwall). (c) Exposure of the fault in a gulley at the base of a ~2-m high fault scarp. (d) Fault exposed along a valley, parallel to the stream trend. (e) Gently dipping alluvial fan displaced by a ~12-m high fault scarp. The scarp can clearly be seen to have collapsed forming a southwest-facing talus slope. The black circle shows a person for scale. (f) Example of a rounded scarp that is ~7-m high with a ~2-m high bedrock scarps along its foot. (g) Displaced alluvial fan gravels underlain by folded Mesozoic rocks. (h) Dark Paleozoic rocks displaced against light alluvial deposits clearly showing the sense of fault dip toward the northeast.

and Paleozoic metamorphic basement. In this region, the IFS had previously been mapped as a reverse fault dipping toward the southwest (INGEMMET, 2017).

We extracted 28 topographic profiles perpendicular to the fault scarps from a high-resolution DEM of the Tauja Zone. The profile locations are indicated in Figures 5b–5d. The scarp heights vary between 0.7 ± 0.1 and 12.0 ± 0.1 m (Figure 5e), with a mean height of 3.1 ± 0.1 m and a median height of 2.3 ± 0.1 m. Similar to the Chintari Zone, most of the scarp heights cluster between 1 and 3 m, while a subset of scarps (24, 25, 26, 27, 28, and 37) are up to 12-m high (Figure 5e). The sense of motion across the Tauja fault scarps is the same as at Chintari and Toquepala, with the north-eastern fault block being uplifted relative to the south-western block.

Bedrock scarps within the Tauja Zone are typically formed in the dark-gray volcaniclastic rocks that have been thrusted over Holocene alluvial gravels. The ~2-m high bedrock scarps have a strike of 251°–275°, a dip of 42°–45° (Figures 6c–6h) and contain slickenlines that pitch 57°–67° toward the northeast (Figures 6a and 6b, inset), indicating that the most recent sense of slip in the Tauja Zone was reverse motion on a north-dipping to northeast-dipping fault with a significant component of left-lateral slip.

Notably the bedrock scarp along this section of the fault often lies at the foot of a taller, rounded scarp (Figures 6e and 6f). In many areas, the uplifted north-eastern block is covered with a thin layer of unconsolidated alluvial gravel and sand which has collapsed over the bedrock scarp, forming a southwest-facing talus slope (Figures 6e and 6g). The southwest-facing slope has previously been interpreted to reflect the fault dip, leading Macharé et al. (2003) to suggest that the most recent sense of slip on the IFS in this region was normal on a southwest-dipping fault. We found that, where the fault plane is well-exposed in stream gullies, it dips toward the northeast (e.g., Figure 6h), confirming that the most recent sense of slip on the IFS in the Tauja Zone was in fact reverse.

A second strand of the IFS has previously been identified in the Tauja Zone within the Rio Sama Valley, between Tarata and Chipispaya Villages (Macharé et al., 2003) (Figure 1, marked "Eastern Toquepala Segment"). The morphological expression of this northern strand is unclear due to extensive fluvial erosion within this high-relief region, but a cross-section through the fault is well-exposed within the banks of the Rio Sama (discussed further in Section 4.2). The exposed fault plane contains slickenlines pitching at 29° toward the ENE on a plane with orientation 280°–292°/37°–53°, indicating the northern strand of the IFS accommodates predominantly left-lateral shear with a minor component of shortening. Notably the sense of motion on this strand of the fault has a much larger strike-slip component than at Toquepala, Chintari, and the southern Tauja Zone, despite the strike and dip of the fault being similar to the other zones. The reasons for the difference in slip vector are unknown.

4.1.4. Santa Elena Zone

The Santa Elena Zone is located at the southeastern end of the traceable fault scarps along the IFS, between the Rio Caplina and the village of Aguas Calientes at the foot of Cerro Tacora (D in Figure 1). In this region, we identified 9 km of subparallel fault scarps that run along the southern side of an E-W striking valley, with north-draining streams having scoured the scarp hanging-walls making the fault clear in optical satellite imagery and DEM relief maps (Figure 7). The IFS is also clear in geological maps of the Santa Elena Zone, where it juxtaposes late Eocene granodiorites northeast of the fault trace against a conformable sequence of Jurassic carbonates southwest of the fault. Near Cerro Santa Elena, the IFS cuts through younger late Cretaceous to Miocene volcaniclastic rocks (INGEMMET, 2017). Throughout this region, the IFS is mapped as a southwest-dipping reverse fault.

We extracted 18 topographic profiles perpendicular to the fault scarps from a high-resolution DEM of the Santa Elena Zone (Figure 7). The profile locations are indicated in Figures 7b–7e. The scarp heights vary between 0.7 ± 0.1 and 9.9 ± 0.1 m (Figure 7f), with a mean height of 3.3 ± 0.1 m and a median height of 2.5 ± 0.1 m. Most of the measured profiles show scarp heights between 1 and 3 m, while 4 profiles record heights >4 m (Figure 7f). The sense of motion across the fault scarps is consistently northeast-up.

Throughout the Santa Elena Zone, many of the >4 m high scarps have heavily rounded crests and a ~2 m high bedrock scarp (Figure 7g), or ~1.5 m escarpments in alluvial deposits (Figure 7h), along their base. The bedrock scarps clearly dip toward the northeast and cut through the alluvial and volcaniclastic drift deposits

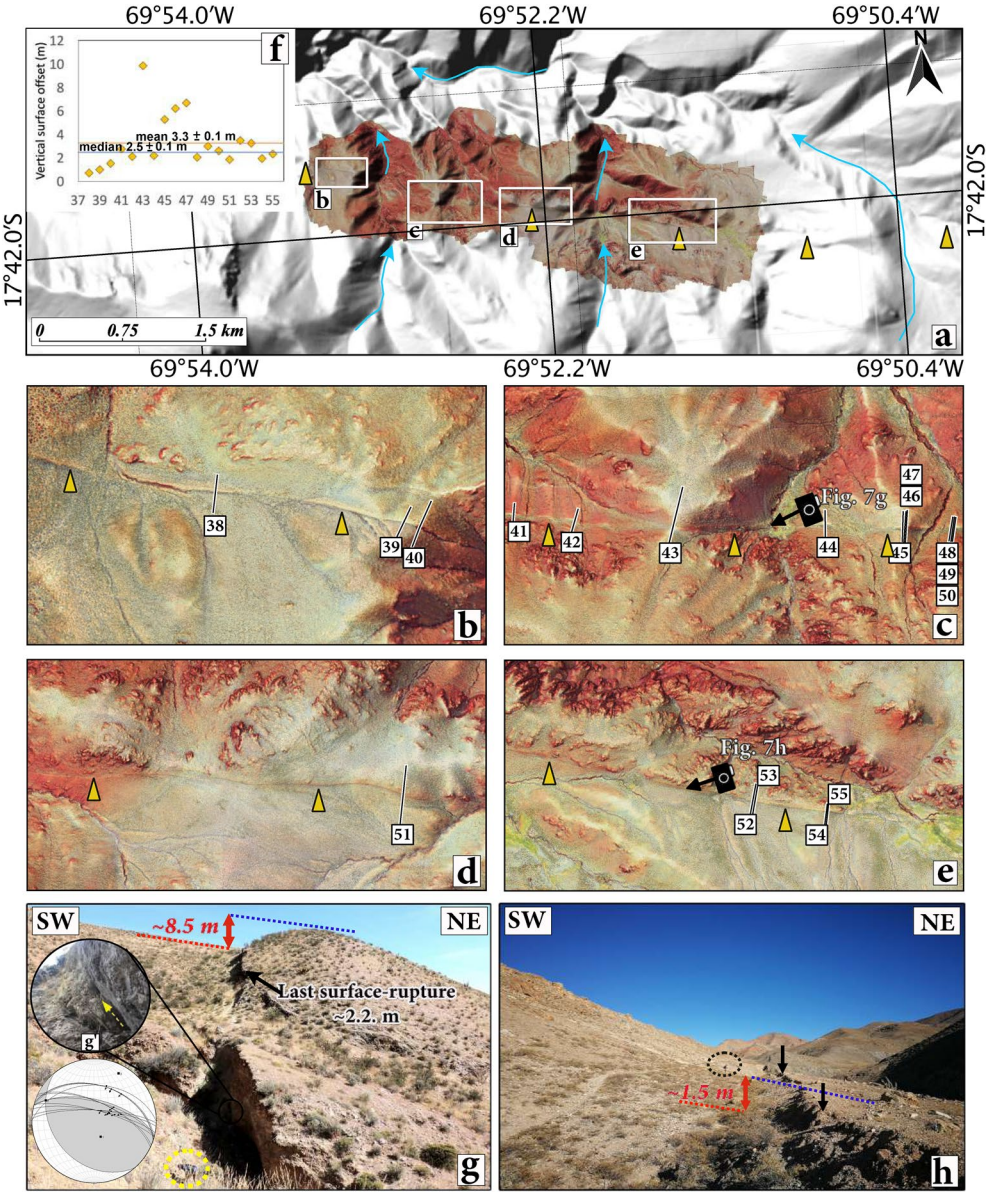

Figure 7. Santa Elena Zone. (a) Background topography from a 12 m Tandem-X DEM overlain by a Red Relief Image Map of the high-resolution DEM. The white rectangles indicate the location of Figures 7b–7e. Yellow triangles mark the fault trace. (b–e) Zoom-in of the Red Relief Image showing the fault scarp morphologies. Black bars indicate the locations of the extracted topography profiles with corresponding numbering. The camera symbols indicate the locations of the photos shown in Figures 7g and 7h. (f) Scarp heights measured from the 18 fault-perpendicular profiles taken across the high-resolution DEM. (g) Photograph of a ~8.5-m high rounded scarp with a ~2-m high bedrock scarp along its foot. A close-up photo of the slickenlines and a stereonet showing their orientation are shown inset. (h) Photograph of a ~1.5-m high scarp near the southern end of the Santa Elena Zone. The black circle shows a person for the scale. DEM, Digital Elevation Models.

that cover bedrock throughout this region. Slickenlines along the exposed bedrock fault surface have an average pitch of 62° toward the northeast on a 285°/70° fault plane, indicating the most recent sense of slip has been reverse motion with a left-lateral component on a steep, northeast-dipping fault plane.

4.1.5. Summary of the Fault Scarp Observations

Between Toquepala and Aguas Calientes we have mapped a cumulative 40 km of NW-SE to E-W trending fault scarps that are intermittently cut by rivers, delineating a ~100 km long fault trace on the IFS. The fault

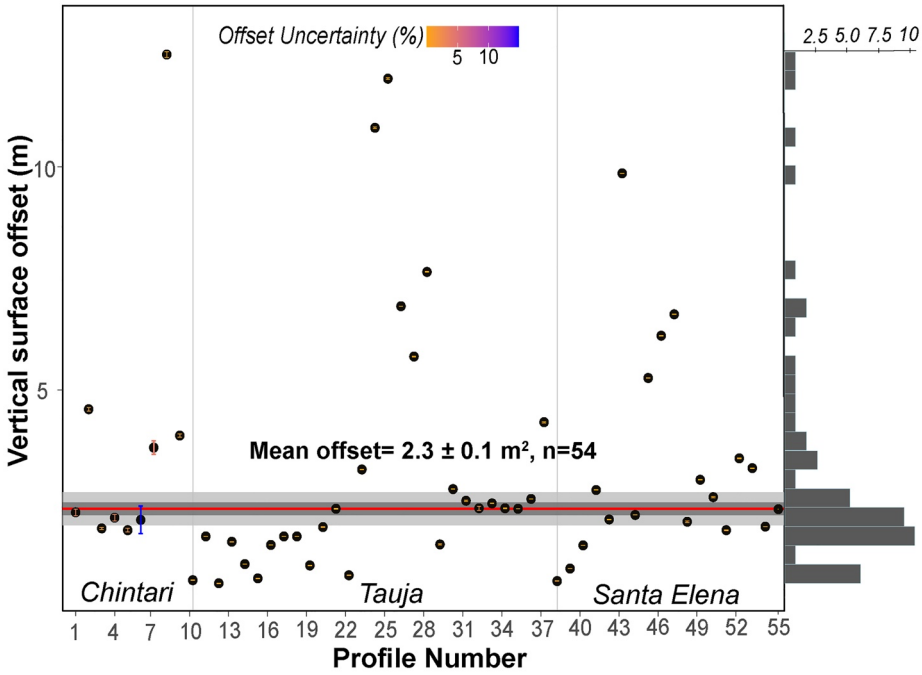

Figure 8. Compilation of the scarp height measurements using topographic profiles perpendicular to the scarp trace with their respective uncertainty. The percentage uncertainty is typically smaller than the symbol size, except for profiles 6 and 8. The red line represents mean displacement of 2.3 ± 0.1 m, and the light-gray band is the 1σ standard deviation. The dark-gray band is the standard error in the estimate of the mean (0.1 m). A histogram of the scarp heights is shown by the gray bars on the right binned in 0.4-m intervals. There is a clear cluster of scarp heights between 2 and 4 m.

scarps have a mean height of 2.3 m, and they mostly cluster between 2 and 4-m high (Figure 8). Some localities preserve taller scarps that reach up to ~14-m high (Figure 8). The taller scarps typically have rounded crests with a fresh, steeply dipping bedrock scarp at their base that offsets the young, unconsolidated alluvial deposits at the surface.

All of the bedrock scarps preserve a sense of slip in the last scarp-forming event of left-lateral transpression on a 40°–70° dipping fault that dips toward the north or northeast beneath the Western Cordillera. We found no evidence for the southwest-dipping fault that appears on most geological maps of the region. The mean azimuth of the slickenlines on the bedrock scarps is 038°.

4.2. Age Constraints on the Incapuquio Fault Scarps

We identified three sites along the IFS suitable for paleoseismological analysis (Figure 1; T1, T2, and T3, respectively). At all of these localities, the fault trace was difficult to access; therefore, we studied natural exposures of the fault with additional hand-dug sections.

The first site (Trench T1—17°34′0.81″S/70°8′50.15″W; Figure 5b) consisted of an exposure within the banks of an incised stream that crosses the fault, exposing a 0.5-m wide, 1.5 m deep cross-section of the fault (Figures 9a and 9b). Within the section, we identified a colluvial wedge consisting of a poorly sorted mixture of light-gray sand and silt with angular pebbles. The wedge fill was distinct from the reddish-brown volcaniclastic bedrock in the fault hanging-wall, and the light-gray, coarse-grained alluvial deposits containing rounded pebble to cobble-sized clasts in the fault footwall. We found no evidence of foliation or clast alignment within the colluvial wedge that might indicate the material had been sheared since its formation. A ~40 cm thick horizontal, light-gray unconsolidated deposit covered the top of the colluvial wedge, and was not offset or deformed by the fault (Figure 9b).

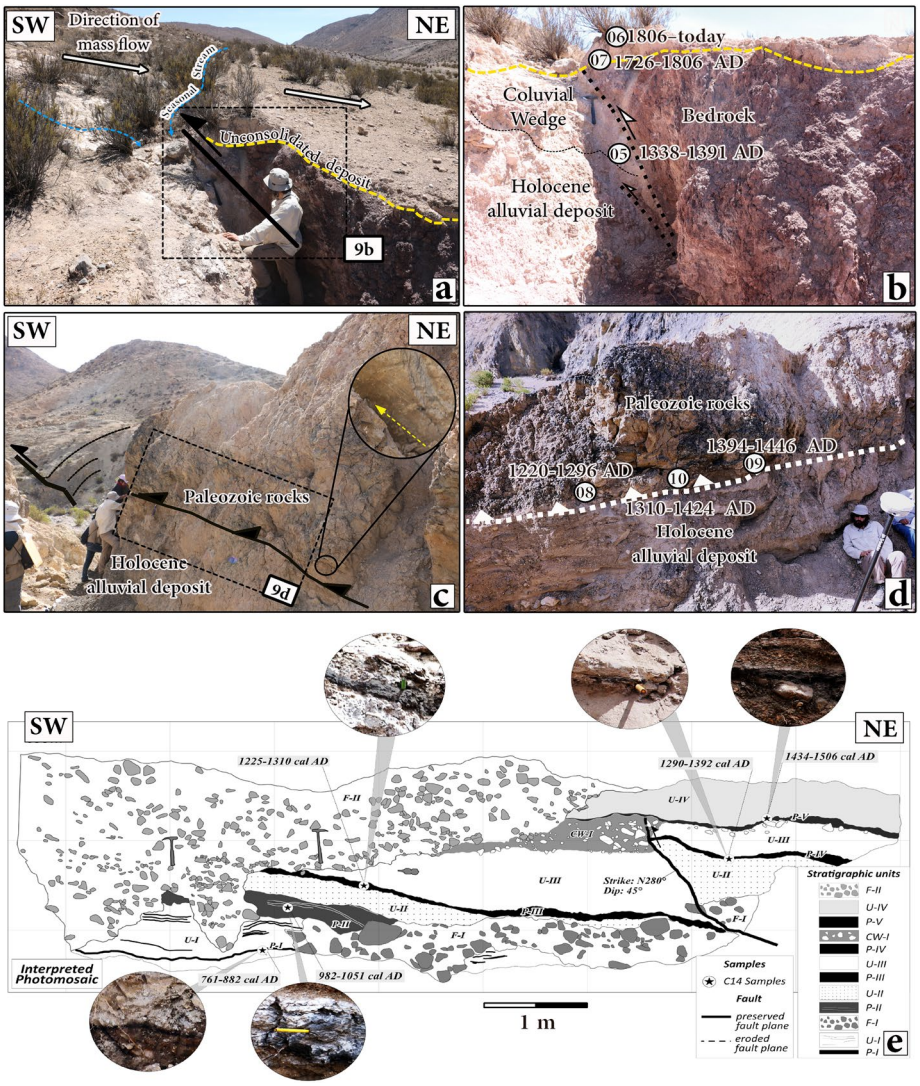

Figure 9. Field photographs of the trenches across the Incapuquio Fault used to estimate the timing of scarp formation. (a) Location of trench T1 where the fault is exposed in a stream gully in the Tauja Zone. The black rectangle corresponds to Figure 9b. (b) Annotated photograph of the fault plane and location of the samples with their respective ages (see description in the main text). (c) Photograph of dark-gray Paleozoic rocks thrust over lighter Holocene deposits at trench site T2. Dead roots used to date the timing of the last slip event in this location were collected from the region of the black-dashed rectangle, which is annotated in Figure 9D. The inset shows detail of the slickenlines on the fault plane in red (see Table S2 and Figure S2). (d) Detailed view of Paleozoic rocks on Holocene gravel with sample locations and with their respective ages (see Table 1). (e) Sketch of the stratigraphy in trench T3. The location and ages of the radiocarbon samples are also shown. The detailed description of the stratigraphic units can be found in Figure S3, as well as the original photomosaic of the trench wall.

We collected three samples from the exposed section for dating (sample details are given in Table 1). A dead root from 20 cm above the base of the colluvial wedge returned a radiocarbon age of 1338–1391 CE (sample: GA50-18-05). Root material from the base and top of the unconsolidated deposit that caps the colluvial wedge returned radiocarbon ages of 1726–1806 CE (sample: GA50-18-07) and 1806 CE-today (sample: GA50-18-06), respectively (Figure 9b). Tephra found within the shallower parts of the colluvial wedge may be from the VEI 6 Plinian eruption of the nearby Huaynaputina volcano in 1600 CE, which generated widespread ash fall within the region and is a common feature of the shallow stratigraphy (Thouret et al., 1999).

When combined together, the radiocarbon dates and the tephra chronology indicate that the colluvial wedge at T1 formed prior to ~1600 CE. However, the lower bound on the timing of scarp formation is less

Table 1
Radiocarbon Dates From the three Studied Zones (IFS)

No.	Sample code	Article code	Material	Site	Conventional age[a]	Calibrated age (Calendric, 2σ)[b]
1	GA50-18-05	05	Wood	Tauja Zone (Trench 1)	700 ± 30 BP	1338–1391 cal AD (52.6%) 1284–1328 cal AD (42.8%)
2	GA50-18-06	06	Wood	Tauja Zone (Trench 1)	120 ± 30 BP	1806–post-AD 1950 (80.3%) 1694–1727 cal AD (15.1%)
3	GA50-18-07	07	Wood	Tauja Zone (Trench 1)	240 ± 30 BP	1726–1806 cal AD (64.9%) 1640–1692 cal AD (30.5%)
4	GA50-18-08	08	Wood	Tauja Zone (Trench 2)	790 ± 30 BP	1220–1296 cal AD (95.4%)
5	GA50-18-09	09	Wood	Tauja Zone (Trench 2)	560 ± 30 BP	1394–1446 cal AD (95.4%)
6	GA50-18-10	10	Wood	Tauja Zone (Trench 2)	620 ± 30 BP	1310–1360 cal AD (49.9%) 1378–1424 cal AD (45.5%)
7	GA50-19-37-T	P-V (Peat V)	Charcoal	Tarata segment (Trench 3)	450 ± 30 BP	1434–1506 cal AD −82.5% 1587–1618 cal AD −12.9%
8	GA50-19-36-T	P-IV (Peat IV)	Charcoal	Tarata segment (Trench 3)	690 ± 30 BP	1290–1392 cal AD −95.4%
9	GA50-19-35-T	P-I (Peat I)	Charcoal	Tarata segment (Trench 3)	1280 ± 30 BP	761–882 cal AD −72.7% 684–740 cal AD −22.7%
10	GA50-19-34-T	P-III (Peat III)	Charcoal	Tarata segment (Trench 3)	770 ± 30 BP	1225–1310 cal AD −88.1% 1360–1379 cal AD −7.3%
11	GA50-19-33-T	P-II (Peat II)	Charcoal	Tarata segment (Trench 3)	1060 ± 30 BP	982–1051 cal AD −76.3% 1080–1144 cal AD

[a]AMS measurements were made at Beta Analytic. [b]Ages were calibrated using OxCal v4.3.2 Bronk Ramsey, (2017) and calibration curve SHCal13 Hogg et al. (2013).

certain. The root material at the base of the colluvial wedge was presumably transported along the surface and into the wedge sometime after the surface rupture formed. The root itself may also have had some residence time on the surface, prior to being transported into the wedge, which may have been large given the hyperarid conditions. However, the residence time can't be greater than ~200–300 years if the base of the wedge must predate 1600 CEand the plant died in ~1338–1391 CE. Therefore, we suggest the surface ruptures formed around ~1200–1500 CE, and were infilled with colluvium and tephra between ~1200–1500 CEand 1600 CE, placing a bound on the timing of the scarp-forming earthquake at this locality.

The second trench site (Trench T2—17°34′22.64″S/70°8′14.78″W; Figure 5b) is another natural exposure in a stream gulley that crosses the fault. The fault trace is marked at the surface by thrusting of pale-brown volcaniclastic bedrock onto light-gray alluvial deposits and recent soils (Figure 9c). Along the margins of the gulley, we identified a 10 cm thick gouge that separates the overthrusting bedrock from the underlying alluvial deposit. The gouge was predominantly formed of material from the underlying alluvium. We collected three dead plant roots from within the gouge (Figures 9d and S1). Radiocarbon dating of these roots yielded relatively consistent ages of 1220–1296 CE (GA50-18-08), 1394–1446 CE (GA50-18-09), and 1310–1424 CE (GA50-18-10) (see Table 1).

If the roots were originally part of the alluvial fan surface, and were incorporated into the fault gouge through shearing during a surface-rupturing earthquake, then the roots should predate the earthquake, and the earthquake must have occurred after 1220–1446 CE. The bound on the timing of the surface-rupturing earthquake at trench site T2 (>1220–1446 CE) overlaps with the bound placed on the colluvial wedge formation at trench site T1 (1200–1500 CE). However, we treat these inferences with caution, as the relative ages of the roots and the fault gouge remain unconstrained.

The third site (Trench T3—17°29′53.77″S/70°11′41.12″W; Figure 1) is located southwest of the town of Tarata, and corresponds to the northern strand of the IFS in the Tauja Zone that was originally mapped by Macharé et al. (2003). At this locality the stratigraphy beneath the fault scarp is exceptionally exposed in a river-cut eroded by the Sama River (Figure S2). We excavated and cleaned the outcrop on the northwest bank forming a 9 m long and 3 m deep exposure (Figure 9e). The deposits in the river bank contain at least five continuous, subhorizontal peat units between 1 and 10 cm thick, some of which are clearly truncated against the fault trace. The peat layers are rich in organic carbon and permit accurate dating of the stratigraphy at this locality.

Radiocarbon ages from five peat samples, three from the footwall, and two from the hanging-wall, place a clear chronology on the stratigraphy and faulting in the trench (Figures 9e and S3). The P-I and P-II peat samples at the lowest stratigraphic level in the trench footwall yielded ages of 761–882 CE (GA50-19-45-T)

and 982–1051 CE (GA50-19-33-T). These dates correlate with two major flood events within the region dated around ~700 CE (Magilligan & Goldstein, 2001) and ~1000 CE (Ortlieb & Macharé, 1993). The P-III and P-IV levels sit higher in the stratigraphy (Figure 9e), and both can be seen to truncate against the fault plane. These two layers have similar stratigraphic characteristics and returned similar, but not equivalent, radiocarbon ages of 1225–1310 CE(GA50-19-34-T) and 1290–1392 CE(GA50-19-36-T), which requires that the fault formed sometime after 1290–1392 CE. If the peat layers P-III and P-IV represent the same stratigraphic level, then they are offset vertically by 0.9 m. Given the highly oblique 29° pitch of slickenlines on the N280°/45°E fault plane exposed nearby, the net slip required to generate this vertical offset is 2.8 m, similar to the net slip required to form the 2–4 m scarp heights seen all along the fault trace described in Section 4.1. A final peat layer P-V that caps the fault, and therefore postdates faulting, yielded a radiocarbon age of 1434–1506 CE (GA50-19-37-T). The high-fidelity chronology afforded by the peat stratigraphy at trench site T3 indicates that slip occurred on this strand of the IFS after 1290–1390 CE, but before 1434–1506 CE.

Using the methodology proposed by Lienkaemper and Ramsey (2009), we built an OxCal stratigraphic model (Bronk Ramsey, 2009) to derive the most probable age of the fault slip event preserved in the stratigraphy at T3 based on the probability density functions of the peat layer radiocarbon ages (Figure 10). We find that fault slip most likely occurred between 1400 and 1440 CE, presumably in a surface-rupturing earthquake. The timing of this earthquake predates the written record of seismicity in the region, which began in ~1500 CE following the Spanish colonization of Perú (Silgado, 1978).

4.3. Recent Seismicity Near the Incapuquio Fault System

Two moderate-magnitude earthquakes with epicenters near the IFS have been recorded by the Global Seismic Network: one event on August 26, 2003 and a second event on the November 20, 2006. A third event occurred offshore the forearc on May 06, 2010. We used teleseismic body-waveform modeling to study the mechanisms and centroid depths of these earthquakes, and compare their kinematics with the recent sense of slip on the IFS.

The August 2003 M_w 5.7 earthquake (Event 1) has compressional *P* wave first motions on vertical-component seismograms at all back-azimuths around the focal sphere suggesting a reverse-faulting mechanism (Figure S4a). The orientation of the nodal planes is well-constrained by changes in the polarity of the *S* and *sS* waves on the transverse seismograms requiring a strike of 220°–250°, a dip of 42°–52°, and a rake of 100°–120°. Notably the strike of both nodal planes is significantly different to the strike of the IFS (~280°–290°) and the possible earthquake slip vectors (NNW or SE) are strongly oblique to the slip vector of slickenlines we have measured from the IFS (NE). The earthquake centroid depth is well-constrained to be 30–34 km by the relative travel time between the *pP*, *sP*, and *sS* phases with the direct phases.

The November 2006 M_w 5.5 earthquake (Event 2) has clear compressional arrivals on the broadband vertical-component seismograms at all back-azimuths around the focal sphere, indicating this was also a reverse-faulting event (Figure S4b). Amplitude variations in the direct *P*-waves require that one of the nodal planes crosses reasonably close on the focal sphere to the stations with azimuths south of the earthquake epicenter. The transverse seismograms are particularly noisy due to the size of the earthquake, but still provide some constraint on the nodal plane orientations due to polarity changes in the direct *S* wave, requiring the strike to be 220°–260°, the dip to be 25°–40°, and the rake to be 40°–90°. As with the 2003 event, both nodal planes are distinctly different to the strike of the IFS (~280°–290°) and the ~N-S slip vector is oblique to that of the IFS (NE). The centroid depth for this earthquake is well-constrained by the differential travel time between the direct and depth phases to be 37–41 km.

The final event in May 2010 (Event 3) ruptured the forearc offshore. This earthquake was an M_w 6.2 reverse-faulting earthquake and was well-recorded by stations surrounding the earthquake epicenter (SupportingInformation Figure S4c). Compressional *P*-wave arrivals at stations of all back-azimuths, and a clear change in the *S*-wave polarity around the focal sphere, require a fault with a strike of 5°–30°, a dip of 35°–45°, and a rake of 95°–125°. Notably the east-dipping nodal plane has a steep dip compared to the east-dipping subduction megathrust earthquakes that commonly occur beneath the forearc. The centroid depth is well-constrained to be 38–42 km.

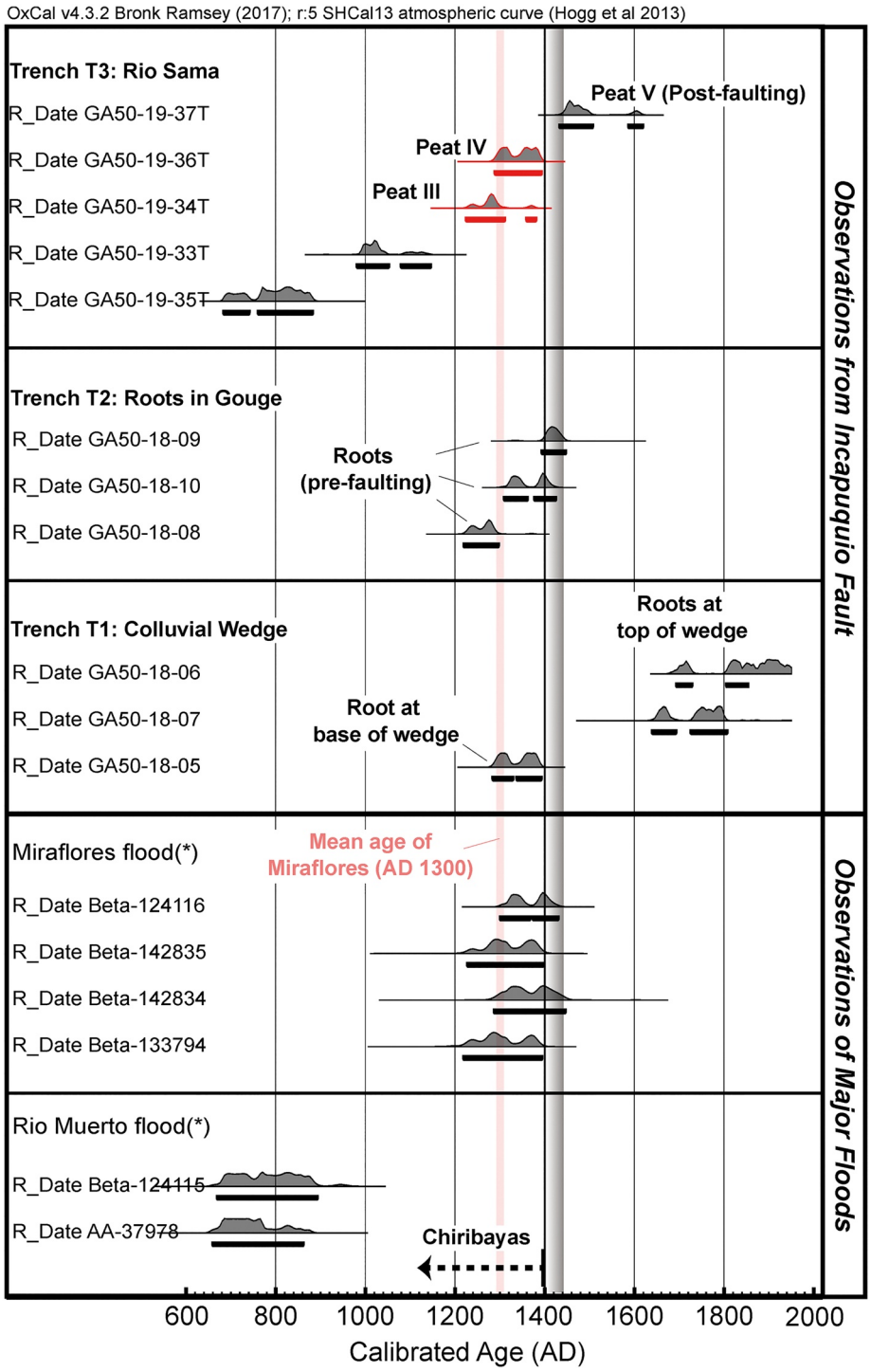

Figure 10. Compilation of the normalized probability density functions of radiocarbon ages from the three trenches discussed in the text and from sediments that date the major flood events in the region based on radiocarbon dating by Magilligan and Goldstein (2001) and Ortlieb and Macharé et al. (1993). The peat layers P-III and P-IV that were offset in trench T3 must predate the scarp-forming earthquake, while the layer P-V must postdate the scarp-forming earthquake, placing the most likely earthquake timing at ~1400–1440 CE (shown by the vertical light-gray band).

5. Discussion

5.1. Interpretation of the Fault Scarp Observations

Fault scarps typically form in surface-rupturing earthquakes, with the along-strike length of the scarps, and the magnitude of the displacement, being related to the earthquake magnitude through empirical scaling relationships derived from modern earthquakes (e.g., Wells & Coppersmith, 1994). A major challenge in applying these scaling relationships to ancient fault scarps is differentiating between scarps that were formed in several different earthquakes, and those formed in a single earthquake.

One way to test whether the IFS scarps were formed in a single earthquake is to study the along-strike distribution of the scarp morphologies and kinematics. We found that the scarps have a consistent ~E-W to ~NW-SE strike, with occasional <1 km left steps in the fault trace. Our scarp height measurements range between 1 and 14 m, though 80% of the scarp heights are between 2 and 4 m. The highest fault scarps are typically heavily rounded along their crests and have a ~2-m high, fresh "scarplet" at their foot. These scarplets are formed in consolidated bedrock, offset the most recent alluvial deposits at the surface, and are of similar height to the mean scarp height (2.3 m) along the IFS.

Slickenlines measured along exposed sections of the fault have similar geometry with a fault plane strike of 245°–290°, a dip of 40°–70°, and a slip vector pitching at 50°–70° toward the northeast. The mean azimuth of the fault slip vector is 038°. Notably, the macroscopic trace of the fault in the satellite data (~300°) has a slightly different strike to our measurements on exposed fault surfaces, as three out of the four measurement sites are along left steps in the fault trace. If the fault slip vector azimuth is consistent along-strike, then left steps in the fault should have a slightly smaller dip-slip component to the slip vector, creating smaller, less prominent scarps. However, we find that the ~30° variability in the fault strike does not contribute significantly to along-strike changes in the scarp heights (Figure 8).

The simplest interpretation of the scarp morphologies and height distribution is that the highest, most rounded scarps are "compound scarps" formed in several surface-rupturing earthquakes. Similar structures have been observed along other faults within the forearc (e.g., the Purgatorio Fault; see Benavente et al., 2017). In some areas, the footwall of the compound scarps has been incised by streams that drain along the fault trace, accentuating their height. The 2–4-m high, fresh scarplet. along the majority of the IFS may therefore have been formed in the most recent surface-rupturing earthquake(s). If the scarps were formed in a single earthquake, we might expect the scarp heights to increase toward the center of the scarp trace (e.g., Middleton et al., 2017). However, we did not find any along-strike trend in the scarp heights (Figure 8).

A second test of whether the IFS scarps formed in a single earthquake, or several earthquakes, is to date the most recent scarp-forming event at different points along-strike. Natural exposures of the stratigraphy at three localities along a 40 km stretch of the IFS point to the most recent surface rupture occurring within a ~300-year period between ~1200 CEand ~1500 CE. At one locality (trench site T3), the timing of most recent surface rupture is well-constrained to be between ~1400 and ~1440 CE. Therefore, it is within the constraints of our dating that the IFS fault scarps formed in a single earthquake, with the most probable timing being between 1400 and 1440 CE. Dating the fault scarps near the ends of the mapped fault trace at Toquepala and Santa Elena would provide an additional test of this hypothesis.

In order to form the 2–4 m high scarps, the net surface slip in the earthquake would have been at least 2.2–4.5 m given the fault dip of 40°–70° and rake of 50°–70°. Using a mean scarp height of 2.3 m, a mean dip of 50°, and a mean rake of 60°, would require a mean fault slip of 3.4 m. It is possible that the true fault dip is toward the larger end of our measurements, as the fault trace is highly linear and there is the possibility for a component of collapse of the fault plane following scarp formation. If we have underestimated the fault dip, then net slip required to form the scarps would be smaller, with a minimum of ~2 m. The cumulative length of the proposed fault rupture is ~100 km, based on the total length of the fault scarps traced between Moquegua and Aguas Calientes. The corresponding fault slip-to-length ratio is $\sim 3 \times 10^{-5}$, and the estimated moment magnitude of the last scarp-forming earthquake would be M_w 7.5 and M_w 7.4 according to the empirical scaling laws of Wells and Coppersmith (1994) and Stirling et al. (2013), respectively. Adding in the 30 km long northern segment of IFS in the Tauja Zone (Macharé et al., 2003) with 2.9 m of slip

would increase the magnitude of this earthquake to M_w 7.7 and M_w 7.5 using the same empirical scaling relationships. Scatter in the scaling relationships would add an uncertainty of 0.1–0.2 magnitude units to these values.

The paleo-magnitude calculations presented above assume that all scarps that have been roughly dated to ~1200–1500 CE ruptured in a single earthquake. Although we consider a single earthquake to be the simplest explanation of the along-strike similarity in scarp heights, scarp morphology, and the fault slip-to-length ratio (Wells & Coppersmith 1994), it is also within the constraints of our dating and fault scarp observations that the fault ruptured in a series of smaller subevents within a ~300-years time period. The magnitudes of these subevents would of course be smaller than ~M_w 7.4–7.7, with their size depending on the level of segmentation. However, modern earthquakes that generate scarps of at least ~2 m are consistently M_w 6.5 or larger (Wells & Coppersmith 1994). Earthquakes of this size still pose a significant hazard to communities that live within ~50–100 km of the fault.

We cannot estimate any recurrence period or long-term slip rate on the IFS from our observations, as there are no correlatable surfaces offset across the taller cumulative scarps that could be reliably dated. Therefore, the regularity of large earthquakes on the IFS remains unknown. Although, given the limited size of the cumulative scarps (10s of meters), the extremely slow erosion rates in the forearc, and the lack of significant kilometer-scale relief change across the IFS, it is likely ruptures on the forearc faults are relatively irregular, and certainly much less frequent than the offshore megathrust earthquakes, which repeat every 150–300 years.

5.2. Deformation in the South Peruvian Forearc

There is growing evidence that Quaternary faulting within the forearc and Western Cordillera of South Perú has variable kinematics in space and time (Audin et al., 2006; Benavente et al., 2017; Binnie et al., 2020; Hall et al., 2012; Loveless et al., 2009; this study). Our observations from the IFS demonstrate that the boundary between the forearc and Western Cordillera failed in at least one large earthquake accommodating left-lateral transpression around 600-years ago (Figure 11a). The ESE-WNW striking Purgatorio and Sama Calientes Faults that lie within the center of the forearc have different kinematics to the IFS. Slickenlines on the near-vertical exposures of the Purgatorio fault plunge 50°–60°, and streams and ridge crests are offset laterally across the fault, indicating late Quaternary right-lateral transpression on this structure (Benavente et al., 2017). Cosmogenic radionuclide dating of surfaces offset by the Purgatorio Fault demonstrate that it has ruptured in the last thousand years (Benavente et al., 2017; Hall et al., 2012). No slickenline measurements have been made on Sama Calientes Fault, though Neogene rocks to the north of the fault trace have been heavily folded and uplifted suggesting it accommodates a component of ~NNE-SSW shortening. Together the Incapuquio, Purgatorio, and Sama Calientes Faults form a conjugate array that may accommodate shortening of the forearc roughly perpendicular to the Perú-Chile trench (Figure 11a).

In contrast, NE-SW striking normal faults (Audin et al., 2006) and surface cracks (Loveless et al., 2009) that lie along the coast at Ilo have accommodated NW-SE trench-parallel extension in the Quaternary (Figure 11a). While south of the Arica Bend, near Pisagua, E-W striking reverse faults accommodate ~N-S trench-parallel shortening (Allmendinger et al., 2005) and ruptured in foreshocks preceding the 2014 Pisagua earthquake (González et al., 2015).

The recent seismicity around the IFS consists of reverse-faulting mechanisms with ~E-W to ~NE-SW striking nodal planes with ~N-S to ~NW-SE trending slip vectors (see Figures 11b and Figures S4a and S4b). Given the mechanisms and depths of the earthquakes, they probably ruptured the base of the brittle part of the forearc wedge above the subduction interface, as moderate-magnitude earthquakes within the subducting slab have depths >50 km east of the coastline and uniformly accommodate ~E-W extension throughout the Arica Bend (Figure 11b), while earthquakes on the subduction interface have low-angle thrust mechanisms with ENE-WSW slip vectors parallel to Nazca-South America relative plate motion. Notably, the possible slip vectors of the two forearc earthquakes studied in Section 4.3 (EV1 and EV2 in Figure 11b) are strongly oblique to the slip vectors measured on the bedrock fault scarps of the Incapuquio Fault, and are reversed relative to the sense of Quaternary extension across the normal faults at Ilo.

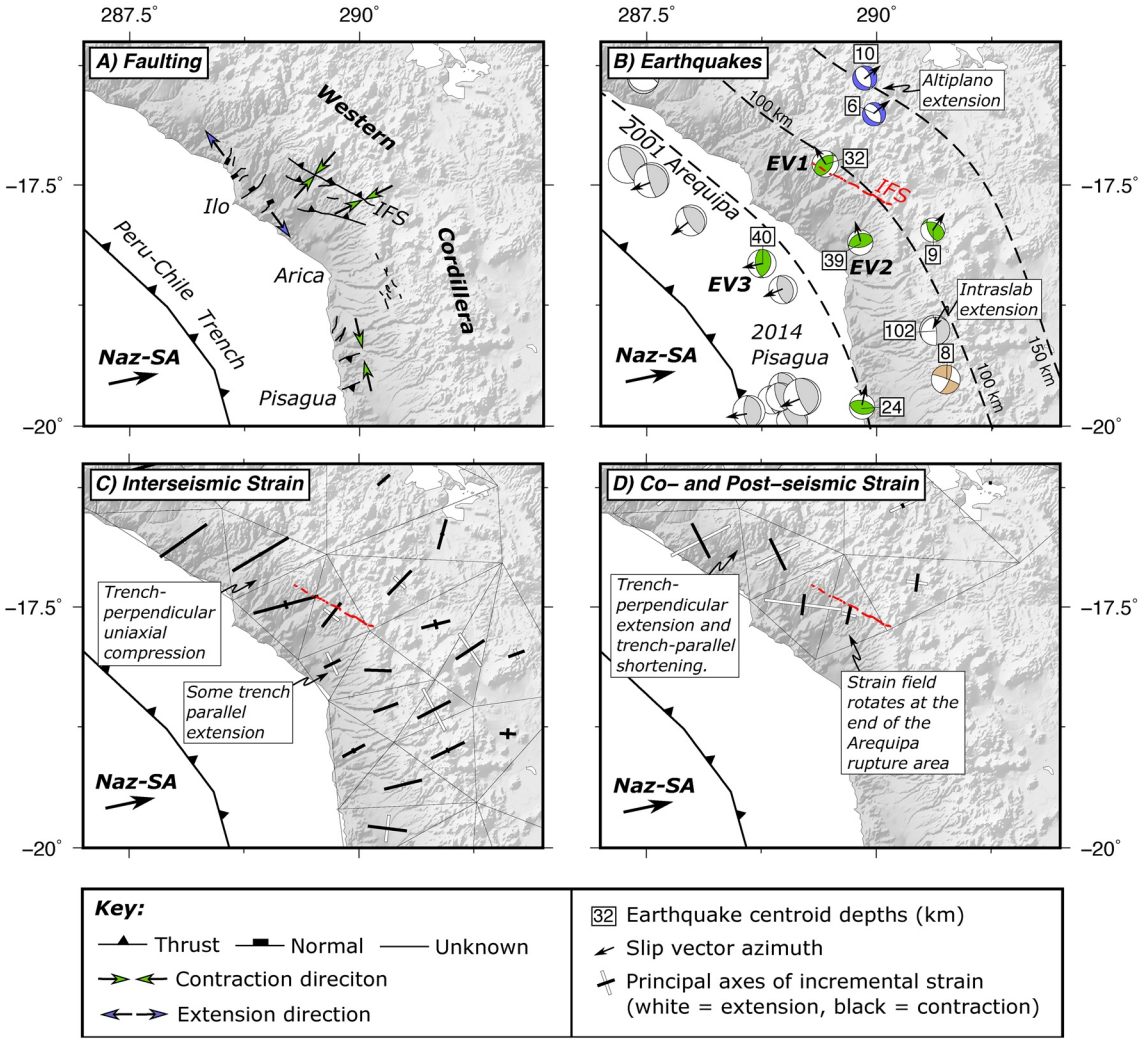

Figure 11. Summary of deformation measurements in the forearc. (a) Active faults mapped in this study and from Audin et al. (2006), Allmendinger et al. (2005), Benavente et al. (2017), and Hall et al. (2012). The direction of relative motion across the fault systems was determined using slickenlines on bedrock fault planes. (b) Focal mechanisms and centroid depths of moderate-magnitude earthquakes ($M_w > 6$ offshore, $M_w > 5.5$ onshore). Light-gray focal mechanisms are from the gCMT catalog (Ekström et al., 2012) and colored focal mechanisms have been studied using teleseismic body-waveform modeling taken from Devlin et al. (2012), Suárez et al. (1983), Wimpenny et al. (2018) and this study (marked EV1, EV2, and EV3). Green mechanisms are reverse faults, brown mechanisms are strike-slip and blue are normal faults. Slip vectors are chosen for the east-dipping plane on the subduction zone, and the south-dipping plane in the overriding plate. The IFS fault scarps are shown in red. Black-dashed lines are contours of the slab surface depth from Slab 2.0 (Hayes et al., 2018). (c) Interseismic strain-rate field calculated using the linear interpolation method of Bourne et al. (1998) with the GPS measurements of Kendrick et al. (2001) collected between 1991 and 2001 prior to the 2001 M_w 8.4 Arequipa earthquake. Triangles in the background represent the Delauney network over which the linear interpolation was performed, with each apex corresponding to a GPS site. (d) Coseismic and early postseismic incremental strain field calculated using the same method and the GPS displacement measurements of Pritchard et al. (2007) collected between 1999 and 2001. No scale is given for the amplitudes of the strain or strain-rate field, as we are only comparing the sense of strain.

The variability in the strikes and slip vectors of the faults and earthquakes near the IFS demonstrate that the kinematics of permanent deformation in the forearc is complex, with evidence for trench-parallel extension, trench-parallel shortening, and trench-perpendicular shortening in close proximity. Similar variability occurs in the pattern of incremental strain within the forearc captured by GPS during the interseismic and coplus postseismic period of the 2001 M_w 8.4 Arequipa earthquake (Figures 11c and 11d). Prior to 2001, the forearc was subject to predominantly ENE-WSW shortening with a minor component of NNW-SSE extension (Allmendinger et al., 2007) (Figure 11c). The principal axis of interseismic shortening was subparallel to the shortening direction on the IFS scarps, while the principal axis of interseismic extension was subparallel to the extension direction across the Ilo normal faults. During and immediately after the 2001 Arequipa

earthquake the incremental strain field reversed, with coseismic and postseismic slip on the megathrust leading to NE-SW extension and NW-SE shortening of the forearc (Figure 11d). Over the same time period, normal-faulting earthquakes in the Altiplano led to NE-SW extension parallel to the principle axis of the coseismic extension (Figure 11b), and two earthquakes ruptured deep in the forearc leading to shortening subparallel to the principle axis of coseismic shortening (Figure 11b).

The GPS and faulting observations are consistent with the paradigm that permanent deformation in the overriding plate is a result of a small fraction of the interseismic strain becoming "sealed in" by slip on forearc faults between megathrust earthquakes (e.g., Allmendinger et al., 2005; Loveless et al., 2010), but also requires that a small fraction of the coseismic and postseismic strain captured by GPS is accommodated by forearc faulting (e.g., Hicks & Rietbrock, 2015). What fraction of the GPS-measured incremental strain will be preserved as permanent deformation in the forearc remains poorly understood, and may well be different between the interseismic, coseismic, and postseismic periods, but could be up to 10% (e.g., Baker et al., 2013).

5.3. Implications for Seismic Hazard

The similarity between the shortening direction across the Incapuquio, Purgatorio, and Sama Calientes Faults, and the principle axis of interseismic shortening in the forearc, suggests that these faults are being loaded toward failure by the compression and torqueing of the overriding plate between megathrust earthquakes (e.g., Loveless et al., 2010). As forearc faults rupture less frequently than the megathrust, elastic strain accumulates within the forearc over several megathrust earthquake cycles. The mechanisms that allow enough strain to accumulate to rupture forearc faults without rupturing the megathrust, presumably the weakest component of subduction system, remain unknown. Nevertheless, faults such as the IFS are more likely to fail after a long-period without a megathrust earthquake, as late in the megathrust earthquake cycle the forearc will be highly compressed, promoting slip on the reverse faults in the forearc (e.g., Loveless et al., 2010). Forearc faults that accommodate deformation with different kinematics to the interseismic strain field, such as the trench-perpendicular reverse faults near the IFS, are not being loaded toward failure between megathrust earthquakes. These faults are more likely to rupture during and immediately after megathrust earthquakes, due to the incremental strain field change related to slip on the subduction interface.

An important implication of this transient compression and stretching of the forearc by the megathrust earthquake cycle is that the seismic hazard posed by any particular forearc fault varies over decadal time scales. Linking the decadal deformation measured by surface GPS to the incremental stress changes on forearc faults could offer a quantitative insight into changes in the possibility of fault rupture (e.g., Loveless et al., 2010; Mildon et al., 2019), but requires improved constraints on the rheological structure of the forearc and its faults. Our waveform-modeling results, in addition to microseismic surveys along the Andean coastline (e.g., Gonzalez et al., 2015), suggest that the forearc can accumulate significant elastic strain and generate earthquakes at depths of at least 40 km, far deeper than the seismicity within the Altiplano, presumably because of the cooling effect of the underthrusting oceanic plate. However, whether the region below 40 km and above the subducting slab deforms seismically or aseismically remains unclear, but will have significant implications for how permanent strain may accumulate in the forearc (e.g., Luo et al., 2019). A thick elastic crust within the forearc may also lead to large but infrequent earthquakes, as the available seismogenic area of fault planes is large. Given how intermittently preserved the fault scarps are along the IFS, despite the scarps occurring in an extremely arid and sparsely populated region, then infrequent but large magnitude earthquakes within the thick brittle crust of other subduction zone forearcs where erosion rates are far higher may be rarely preserved, and therefore overlooked as a source of seismic hazard (e.g., Astudillo-Sotomayor et al., 2021).

5.4. Collapse of the Chiribaya Civilization Around the 1400–1440 CE Earthquake

A number of different civilizations have thrived and collapsed in the hyperarid forearc around the Incapuquio Fault over the last ~4 kyr (Goldstein & Magilligan, 2011). These civilizations based their fresh water supply on sophisticated irrigation systems and canals that drained water from the Western Cordillera

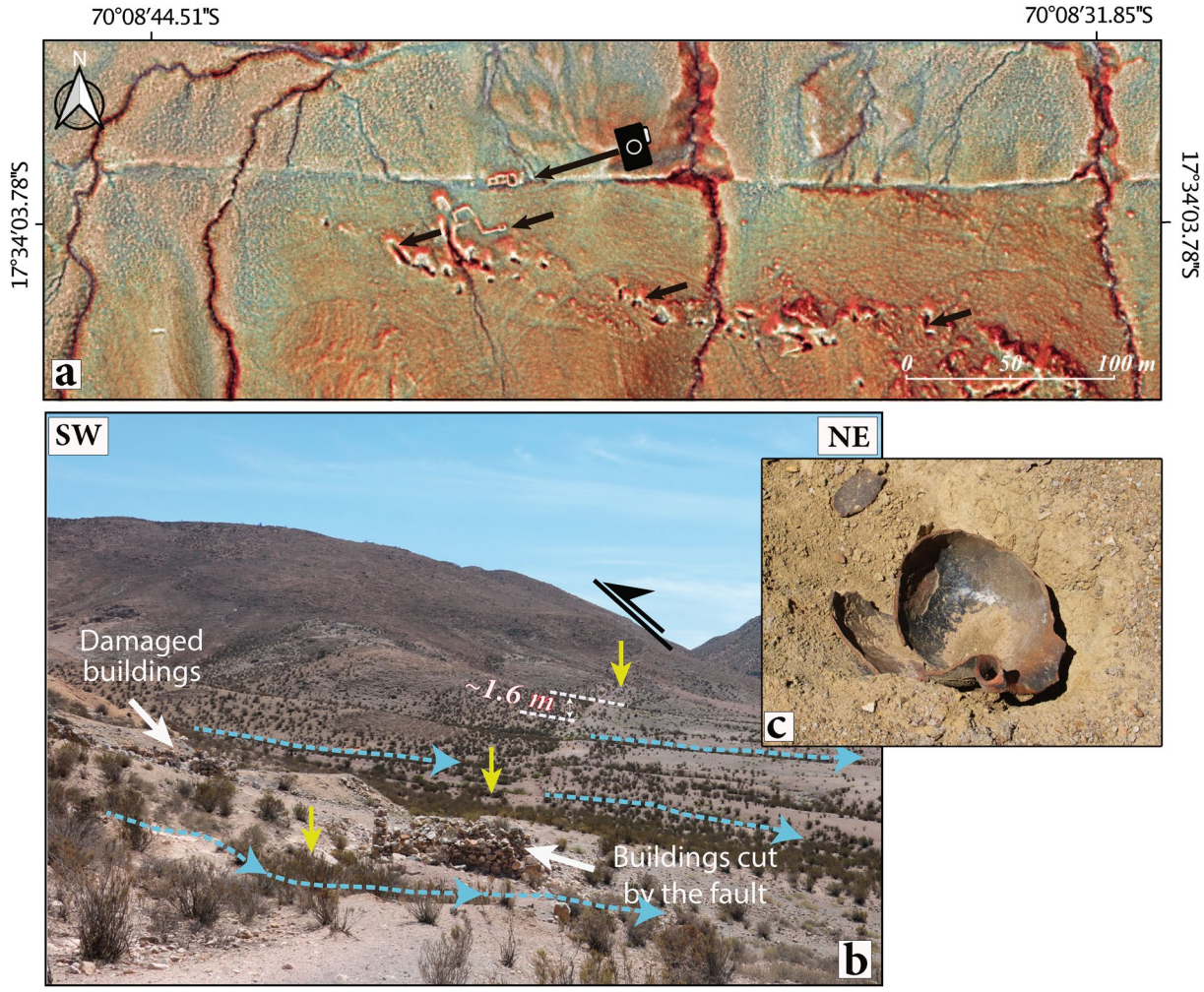

Figure 12. Damaged building associated with faulting in the Tauja Zone. (a) Red Relief Image Map of damaged buildings on the IFS, which are highlighted with black arrows (see location in Figure 5b). Given the style of the buildings, and the fact they are cut by the fault scarp, we hypothesize that they correspond to the Chiribaya civilization (Reycraft, 1998). (b) Field photograph of the buildings that cut by the fault scarp, which are now destroyed. (c) Damaged ceramics found within the confines of the buildings. Detailed archeological surveys of this site may be able to more accurately distinguish its provenance. IFS, Incapuquio Fault System.

into the arid forearc (e.g., Zaro et al., 2013). Consequently, it is often argued that exceptional rainfall, or destruction of the irrigation systems, was the main driver of the decline of ancient populations in the region. For example, Keefer et al. (2003) and Wells (1990) suggested that large floods associated with El Niño Southern Oscillation in ~1330 CE (known as the Miraflores flood) may have contributed to a ~70–80% decline in the population of the Chiribaya civilization of the Moquegua Valley (Figure 1) between 1360 and 1400 CE. However, Clement and Moseley (1991) argue that a famine in the nearby Carrizal valley around 1360–1400 CE is incompatible with a mega-Niño event. In addition, Zaro et al. (2013) argue that the Chiribayas adapted to the variable hydrological specificities of the Andean rivers, and that the Miraflores event alone may not be the trigger of the Chiribayas collapse. As no evidence for shallow-crustal earthquakes have been previously reported in this region, earthquake-related damage or deaths have not been considered as a potential influence on the collapse of the Chiribaya civilization.

During our field reconnaissance, we found collapsed structures such as terraces, storehouses, roads, aqueducts, and corrals in close proximity to the fault scarps on the IFS. In the Tauja Zone, we also identified buildings cut by the main scarp of the IFS with a net displacement of 1.6 m (Figure 12). Although we do not know the exact age of these buildings, we hypothesize that they are from the Chiribaya period, based on the type of buildings, ceramics (Reycraft, 1998) and the observation that the ~1400–1440 CEscarp cuts some of

these structures so must postdate them. Although a provocative proposal, it is possible that infrastructure damage generated by a major earthquake along the IFS around 1400–1440 CE contributed to the decline of the Chiribayas. We stress that further archeological and geological investigation is required to test this hypothesis.

6. Conclusions

We have presented evidence that 2–4 m high fault scarps were formed by a transpressional earthquake that ruptured 100 km of the southern segment of the Incapuquio Fault System in the early 15th century (~1400–1440 CE). Empirical scaling relationships suggest the magnitude of this earthquake could have been M_w 7.4–7.7 with at least 2–3 m of net slip. Recurrence of similar events pose a significant hazard to the population living in the forearc region of Perú. The timing of this earthquake coincides with the collapse of the population of the Chiribaya civilization between ~1360 and 1400 CE, and we present evidence of damaged and offset buildings along the fault trace that may be of Chiribayas age. The kinematics of the Incapuquio Fault suggest that it ruptures following the accumulation of compressional elastic strain in the forearc during the interseismic period of the megathrust earthquake cycle. Many other active faults within the forearc with different strikes and slip vectors to the Incapuquio Fault imply that permanent deformation in the region is complex, probably due to the time-varying stress field within the overriding plate caused by megathrust earthquakes.

Data Availability Statement

The drone DEMs are freely available through OpenTopography (www.opentopography.org) at https://doi.org/10.5069/G9JW8C3S (Chintari Zone), https://doi.org/10.5069/G9TD9VH0 (Tauja Zone) and https://doi.org/10.5069/G9PN93T3 (Santa Elena Zone). All other data used in this study are provided in the text.

Acknowledgments
This work was part of INGEMMET's research and was funded through the GA-50 project "Neotectonic Studies in Peru." We wish to thank Jorge Basadre Grohmann University in Tacna for their assistance during this work. S. Wimpenny was supported by the Denman Baynes Junior Research Fellowship at Clare College, Cambridge. X. Robert was supported by the Institut de Recherche pour le Développement (IRD) through BQR-SUD 2018 funds from ISTerre Lab and expatriation program. The supporting information contains figures of the topography profiles across the fault scarp and further information about the body-waveform modeling. We acknowledge the work of the Associate Editor Laura Giambiagi, and two anonymous reviewers for their constructive comments.

References

Allmendinger, R. (2018). *Software FaultKin 8*. Retrieved from http://www.geo.cornell.edu/geology/faculty/RWA/programs/faultkin.html

Allmendinger, R. W., González, G., Yu, J., Hoke, G., & Isacks, B. (2005). Trench-parallel shortening in the northern Chilean Forearc: Tectonic and climatic implications. *Geological Society of America Bulletin*, *117*(1–2), 89–104. https://doi.org/10.1130/b25505.1

Allmendinger, R. W., Reilinger, R., & Loveless, J. (2007). Strain and rotation rate from GPS in Tibet, Anatolia, and the Altiplano. *Tectonics*, *26*, TC3013. https://doi.org/10.1029/2006TC002030

Armijo, R., Lacassin, R., Coudurier-Curveur, A., & Carrizo, D. (2015). Coupled tectonic evolution of Andean orogeny and global climate. *Earth-Science Reviews*, *143*, 1–35. https://doi.org/10.1016/j.earscirev.2015.01.005

Astudillo-Sotomayor, L., Jara-Muñoz, J., Melnick, D., Cortés-Aranda, J., Tassara, A., & Strecker, M. R. (2021). Fast Holocene slip and localized strain along the Liquiñe-Ofqui strike-slip fault system, Chile. *Scientific Reports*, *11*(1), 5970. https://doi.org/10.1038/s41598-021-85036-5

Audin, L., David, C., Hall, S., Farber, D., & Hérail, G. (2006). Geomorphic evidences of recent tectonic activity in the forearc, southern Peru. *Revista de la Asociación Geológica Argentina*, *61*(4), 545–554.

Baker, A., Allmendinger, R. W., Owen, L. A., & Rech, J. A. (2013). Permanent deformation caused by subduction earthquakes in northern Chile. *Nature Geoscience*, *6*(6), 492–496. https://doi.org/10.1038/ngeo1789

Bellido, E. (1979). *Geología del cuadrángulo de Moquegua 35-u-[Boletín A 15]*. Instituto Geológico, Minero y Metalúrgico-INGEMMET. Retrieved from https://repositorio.ingemmet.gob.pe/handle/20.500.12544/132

Benavente, C., Delgado, F., García Fernández Baca, B., Alegre, E., & Audin, L. (2018). *Neotectónica, evolución del relieve y peligro sísmico en la región Arequipa-[Boletín C 64]*. Instituto Geológico, Minero y Metalúrgico-INGEMMET. Retrieved from http://repositorio.ingemmet.gob.pe/handle/ingemmet/1223

Benavente, C., Delgado, F., Taipe, E., Audin, L., & Pari, W. (2013). *Neotectonica y Peligro Sismico en el Region Cusco* (pp. 245). INGEMMET.

Benavente, C., Zerathe, S., Audin, L., Hall, S. R., Robert, X., Delgado, F., et al. (2017). Active transpressional tectonics in the Andean forearc of southern Peru quantified by ^{10}Be surface exposure dating of an active fault scarp. *Tectonics*, *36*, 1662–1678. https://doi.org/10.1002/2017TC004523

Binnie, S. A., Reicherter, K. R., Victor, P., González, G., Binnie, A., Niemann, K., et al. (2020). The origins and implications of paleochannels in hyperarid, tectonically active regions: The northern Atacama Desert, Chile. *Global and Planetary Change*, *185*, 103083. https://doi.org/10.1016/j.gloplacha.2019.103083

Bourne, S. J., Árnadóttir, T., Beavan, J., Darby, D. J., England, P. C., Parsons, B., et al. (1998). Crustal deformation of the Marlborough fault zone in the South Island of New Zealand: Geodetic constraints over the interval 1982–1994. *Journal of Geophysical Research*, *103*(B12), 30147–30165. https://doi.org/10.1029/98JB02228

Bronk Ramsey, C. (2009). Bayesian analysis of radiocarbon dates. *Radiocarbon*, *51*(1), 337–360. https://doi.org/10.1017/s0033822200033865

Bronk Ramsey, C. B. (2017). Methods for summarizing radiocarbon datasets. *Radiocarbon*, *59*(6), 1809–1833. https://doi.org/10.1017/rdc.2017.108

Chiba, T., Suzuki, Y., & Hiramatsu, T. (2007). Digital terrain representation methods and red relief image map: A new visualization approach Map. *Journal of the Japan Cartographers Association*, *45*(1), 27–36. https://doi.org/10.11212/jjca1963.45.27

Clement, C. O., & Moseley, M. E. (1991). The spring-fed irrigation system of Carrizal, Peru: A case study of the hypothesis of agrarian collapse. *Journal of Field Archaeology*, *18*(4), 425–443. https://doi.org/10.2307/530406

David, C., Audin, L., Comte, D., Tavera, H., & Hérail, G. (2005). Crustal seismicity and active tectonics in the Arica bend forearc. Paper presented at *6th International Symposium on Andean Geodynamics: Extended abstracts* (Vol. 6, pp. 206–210). Barcelone (ESP): IRD. Retrieved from http://www.documentation.ird.fr/hor/fdi:010040208

DeMets, C., Gordon, R. G., & Argus, D. F. (2010). Geologically current plate motions. *Geophysical Journal International*, *181*(1), 1–80. https://doi.org/10.1111/j.1365-246x.2009.04491.x

Devlin, S., Isacks, B. L., Pritchard, M. E., Barnhart, W. D., & Lohman, R. B. (2012). Depths and focal mechanisms of crustal earthquakes in the central Andes determined from teleseismic waveform analysis and InSAR: Crustal earthquakes of the Central Andes. *Tectonics*, *31*, TC2002. https://doi.org/10.1029/2011TC002914

Dorbath, L., Cisternas, A., & Dorbath, C. (1990). Assessment of the size of large and great historical earthquakes in Peru. *Bulletin of the Seismological Society of America*, *80*(3), 551–576.

Dunai, T. J., González López, G. A., & Juez-Larré, J. (2005). Oligocene-Miocene age of aridity in the Atacama Desert revealed by exposure dating of erosion-sensitive landforms. *Geology*, *33*(4), 321–324. https://doi.org/10.1130/g21184.1

Ekström, G., Nettles, M., & Dziewoński, A. M. (2012). The global CMT project 2004–2010: Centroid-moment tensors for 13,017 earthquakes. *Physics of the Earth and Planetary Interiors*, *200–201*, 1–9. https://doi.org/10.1016/j.pepi.2012.04.002

Garzione, C. N., McQuarrie, N., Perez, N. D., Ehlers, T. A., Beck, S. L., Kar, N., et al. (2017). Tectonic evolution of the central Andean Plateau and implications for the growth of plateaus. *Annual Review of Earth and Planetary Sciences*, *45*(1), 529–559. https://doi.org/10.1146/annurev-earth-063016-020612

Goldstein, P. S., & Magilligan, F. J. (2011). Hazard, risk and agrarian adaptations in a hyperarid watershed: El Niño floods, streambank erosion, and the cultural bounds of vulnerability in the Andean Middle Horizon. *Catena*, *85*(2), 155–167. https://doi.org/10.1016/j.catena.2010.11.001

González, G., Salazar, P., Loveless, J. P., Allmendinger, R. W., Aron, F., & Shrivastava, M. (2015). Upper plate reverse fault reactivation and the unclamping of the megathrust during the 2014 northern Chile earthquake sequence. *Geology*, *43*(8), 671–674. https://doi.org/10.1130/g36703.1

Grützner, C. H., Carson, E., Walker, R. T., Rhodes, E. J., Mukambayev, A., Mackenzie, D., et al. (2017). Assessing the activity of faults in continental interiors: Palaeoseismic insights from SE Kazakhstan. *Earth and Planetary Science Letters*, *459*, 93–104. https://doi.org/10.1016/j.epsl.2016.11.025

Hall, S. R., Farber, D. L., Audin, L., & Finkel, R. C. (2012). Recently active contractile deformation in the forearc of southern Peru. *Earth and Planetary Science Letters*, *337–338*, 85–92. https://doi.org/10.1016/j.epsl.2012.04.007

Hamling, I. J., Hreinsdóttir, S., Clark, K., Elliott, J., Liang, C., Fielding, E., et al. (2017). Complex multifault rupture during the 2016 M_w 7.8 Kaikōura earthquake, New Zealand. *Science*, *356*(6334), eaam7194. https://doi.org/10.1126/science.aam7194

Hayes, G. P., Moore, G. L., Portner, D. E., Hearne, M., Flamme, H., Furtney, M., & Smoczyk, G. M. (2018). Slab2: A comprehensive subduction zone geometry model. *Science*, *362*(6410), 58–61. https://doi.org/10.1126/science.aat4723

Hicks, S. P., & Rietbrock, A. (2015). Seismic slip on an upper-plate normal fault during a large subduction megathrust rupture. *Nature Geoscience*, *8*(12), 955–960. https://doi.org/10.1038/ngeo2585

Hogg, A. G., Hua, Q., Blackwell, P. G., Niu, M., Buck, C. E., Guilderson, T. P., et al. (2013). SHCal13 southern hemisphere calibration, 0-50,000 years cal BP. *Radiocarbon*, *55*(4), 1889–1903. https://doi.org/10.2458/azu_js_rc.55.16783

Horton, B. K., Hampton, B. A., & Waanders, G. L. (2001). Paleogene synorogenic sedimentation in the Altiplano plateau and implications for initial mountain building in the central Andes. *Geological Society of America Bulletin*, *113*, 1387–1400. https://doi.org/10.1130/0016-7606(2001)113<1387:pssita>2.0.co;2

Isacks, B. L. (1988). Uplift of the Central Andean Plateau and bending of the Bolivian Orocline. *Journal of Geophysical Research*, *93*(B4), 3211–3231. https://doi.org/10.1029/JB093iB04p03211

Jacay, J., Sempéré, T., Husson, L., Pino, A., & ISAG. International Symposium on Andean Geodynamics, 5., Toulouse (FRA), 2002/09/16-18 (2002). Structural characteristics of the Incapuquio fault system, southern Peru. In *Andean geodynamics: Extended abstracts* (pp. 319–321). Paris: IRD. Retrieved from http://www.documentation.ird.fr/hor/fdi:010047938

Jaillard, E., Hérail, G., Monfret, T., & Wörner, G. (2002). *Andean geodynamics: Main issues and contributions from the 4th ISAG*. Göttingen: Elsevier.

Keefer, D. K., Moseley, M. E., & DeFrance, S. D. (2003). A 38,000-year record of floods and debris flows in the Ilo region of southern Peru and its relation to El Niño events and great earthquakes. *Palaeogeography, Palaeoclimatology, Palaeoecology*, *194*(1–3), 4177. https://doi.org/10.1016/s0031-0182(03)00271-2

Kendrick, E., Bevis, M., Smalley, R., & Brooks, B. (2001). An integrated crustal velocity field for the central Andes. *Geochemistry, Geophysics, Geosystems*, *2*(11), 1066. https://doi.org/10.1029/2001GC000191

Lienkaemper, J. J., & Ramsey, C. B. (2009). OxCal: Versatile tool for developing paleoearthquake chronologies—A primer. *Seismological Research Letters*, *80*(3), 431–434. https://doi.org/10.1785/gssrl.80.3.431

Loveless, J. P., Allmendinger, R. W., Pritchard, M. E., Garroway, J. L., & González, G. (2009). Surface cracks record long-term seismic segmentation of the Andean margin. *Geology*, *37*(1), 23–26. https://doi.org/10.1130/g25170a.1

Loveless, J. P., Allmendinger, R. W., Pritchard, M. E., & González, G. (2010). Normal and reverse faulting driven by the subduction zone earthquake cycle in the northern Chilean fore arc. *Tectonics*, *29*, TC2001. https://doi.org/10.1029/2009TC002465

Luo, H., Wang, K., Sone, H., & He, J. (2019). A model of shallow viscoelastic relaxation for seismically induced tension cracks in the Chile-Peru forearc. *Geophysical Research Letters*, *46*, 10773–10781. https://doi.org/10.1029/2019GL084536

Macharé, J., Fenton, C. H., Machette, M. N., Lavenu, A., Costa, C., & Dart, R. L. (2003). Database and map of quaternary faults and folds in Peru and its offshore region. In *Database and Map of Quaternary Faults and Folds in Peru and its Offshore Region* (Vol. *2003-451*). USGS Numbered Series. https://doi.org/10.3133/ofr03451

Macharé Ordoñez, J., Benavente Escobar, B., & Audin, L. (2009). *Síntesis descriptiva del mapa neotectónico 2008-[Boletín C 40]*. Retrieved from http://repositorio.ingemmet.gob.pe/handle/ingemmet/245

Mackenzie, D., & Elliott, A. (2017). Untangling tectonic slip from the potentially misleading effects of landform geometry. *Geosphere*, *13*(4), 1310–1328. https://doi.org/10.1130/GES01386.1

Magilligan, F. J., & Goldstein, P. S. (2001). El Niño floods and culture change: A late Holocene flood history for the Rio Moquegua, southern Peru. *Geology*, *29*(5), 431–434. https://doi.org/10.1130/0091-7613(2001)029<0431:enofac>2.0.co;2

McCaffrey, R., & Abers, G. (1988). *SYN3: A program for inversion of teleseismic body waveform on microcomputers* (Tech. Rep. AFGL-TR-88-0099). Air Force Geophysics Laboratory. https://doi.org/10.21236/ada198940

McCalpin, J. P. (2009). *Paleoseismology*. Academic Press.
McQuarrie, N., Horton, B. K., Zandt, G., Beck, S., & DeCelles, P. G. (2005). Lithospheric evolution of the Andean fold-thrust belt, Bolivia, and the origin of the central Andean plateau. *Tectonophysics*, *399*(1–4), 15–37. https://doi.org/10.1016/j.tecto.2004.12.013
Middleton, T. A., Elliott, J. R., Rhodes, E. J., Sherlock, S., Walker, R. T., Wang, W., et al. (2017). Extension rates across the northern Shanxi Grabens, China, from Quaternary geology, seismicity and geodesy. *Geophysical Journal International*, *209*(2), 535–558.
Mildon, Z. K., Roberts, G. P., Faure Walker, J. P., & Toda, S. (2019). Coulomb pre-stress and fault bends are ignored yet vital factors for earthquake triggering and hazard. *Nature Communications*, *10*(1), 2744. https://doi.org/10.1038/s41467-019-10520-6
Molnar, P., & Lyon-Caent, H. (1989). Fault plane solutions of earthquakes and active tectonics of the Tibetan Plateau and its margins. *Geophysical Journal International*, *99*(1), 123–154. https://doi.org/10.1111/j.1365-246x.1989.tb02020.x
Morell, K. D., Regalla, C., Amos, C., Bennett, S., Leonard, L., Graham, A., et al. (2018). Holocene surface rupture history of an active forearc fault redefines seismic hazard in Southwestern British Columbia, Canada. *Geophysical Research Letters*, *45*, 11605–11611. https://doi.org/10.1029/2018GL078711
Norton, K., & Schlunegger, F. (2011). Migrating deformation in the Central Andes from enhanced orographic rainfall. *Nature Communications*, *2*, 584. https://doi.org/10.1038/ncomms1590
Ortlieb, L., & Macharé, J. (1993). Former El Niño events: Records from western South America. *Global and Planetary Change*, *7*(1–3), 181–202. https://doi.org/10.1016/0921-8181(93)90049-t
Pritchard, M. E., Norabuena, E. O., Ji, C., Boroschek, R., Comte, D., Simons, M., et al. (2007). Geodetic, teleseismic, and strong motion constraints on slip from recent southern Peru subduction zone earthquakes. *Journal of Geophysical Research*, *112*, B03307. https://doi.org/10.1029/2006JB004294
Ramos, V. A. (2010). The tectonic regime along the Andes: Present-day and Mesozoic regimes. *Geological Journal*, *45*(1), 2–25. https://doi.org/10.1002/gj.1193
Reycraft, R. M. (1998). *The terminal Chiribaya project: The archaeology of human response to natural disaster in South coastal Peru*. The University of New Mexico, ProQuest Dissertations.
Rizzoli, P., Martone, M., Gonzalez, C., Wecklich, C., Borla Tridon, D., Bräutigam, B., et al. (2017). Generation and performance assessment of the global TanDEM-X digital elevation model. *ISPRS Journal of Photogrammetry and Remote Sensing*, *132*, 119–139. https://doi.org/10.1016/j.isprsjprs.2017.08.008
Schermer, E. R., Amos, C. B., Duckworth, W. C., Nelson, A. R., Angster, S., & Sherrod, B. L. (2020). Postglacial *Mw* 7.0–7.5 Earthquakes on the north Olympic Fault Zone, Washington. *Bulletin of the Seismological Society of America*, *111*(1), 490–513. https://doi.org/10.1785/0120200176
Schildgen, T. F., Hodges, K. V., Whipple, K. X., Reiners, P. W., & Pringle, M. S. (2007). Uplift of the western margin of the Andean plateau revealed from canyon incision history, southern Peru. *Geology*, *35*(6), 523–526. https://doi.org/10.1130/g23532a.1
Schildgen, T. F., Hodges, K. V., Whipple, K. X., Pringle, M. S., van Soest, M., & Cornell, K. (2009). Late Cenozoic structural and tectonic development of the western margin of the central Andean Plateau in southwest Peru. *Tectonics*, *28*, TC4007. https://doi.org/10.1029/2008TC002403
Sébrier, M., Mercier, J. L., Mégard, F., Laubacher, G., & Carey-Gailhardis, E. (1985). Quaternary normal and reverse faulting and the state of stress in the central Andes of south Peru. *Tectonics*, *4*(7), 739–780. https://doi.org/10.1029/TC004i007p00739
Silgado, E. (1978). Historia de los sismos más notables ocurridos en el Perú (1513–1974). *Serie C. Geodinámica e Ingeniería Geológica, 3*. Instituto de Geología y Minería.
Stirling, M., Goded, T., Berryman, K., & Litchfield, N. (2013). Selection of earthquake scaling relationships for Seismic-Hazard Analysis. *Bulletin of the Seismological Society of America*, *103*(6), 2993–3011. https://doi.org/10.1785/0120130052
Suárez, G., Molnar, P., & Burchfiel, B. C. (1983). Seismicity, fault plane solutions, depth of faulting, and active tectonics of the Andes of Peru, Ecuador, and southern Colombia. *Journal of Geophysical Research*, *88*(B12), 10403–10428. https://doi.org/10.1029/JB088iB12p10403
Thouret, J.-C., Davila, J., & Eissen, J.-P. (1999). Largest explosive eruption in historical times in the Andes at Huaynaputina volcano, A.D. 1600, southern Peru. *Geology*, *27*(5), 435–438. https://doi.org/10.1130/0091-7613(1999)027<0435:leeiht>2.3.co;2
Villegas-Lanza, J. C., Chlieh, M., Cavalié, O., Tavera, H., Baby, P., Chire-Chira, J., & Nocquet, J.-M. (2016). Active tectonics of Peru: Heterogeneous interseismic coupling along the Nazca megathrust, rigid motion of the Peruvian Sliver, and Subandean shortening accommodation. *Journal of Geophysical Research: Solid Earth*, *121*, 7371–7394. https://doi.org/10.1002/2016JB013080
Wells, D. L., & Coppersmith, K. J. (1994). New empirical relationships among magnitude, rupture length, rupture width, rupture area, and surface displacement. *Bulletin of the Seismological Society of America*, *84*(4), 974–1002.
Wells, L. E. (1990). Holocene history of the El Niño phenomenon as recorded in flood sediments of northern coastal Peru. *Geology*, *18*(11), 1134–1137. https://doi.org/10.1130/0091-7613(1990)018<1134:hhoten>2.3.co;2
Westoby, M. J., Brasington, J., Glasser, N. F., Hambrey, M. J., & Reynolds, J. M. (2012). 'Structure-from-Motion' photogrammetry: A low-cost, effective tool for geoscience applications. *Geomorphology*, *179*, 300–314. https://doi.org/10.1016/j.geomorph.2012.08.021
Wilson, J. J., & García, W. (1962). *Geología de los cuadrángulos de Pachia y Palca (Hojas 36-v y 36-x)-[Boletin A 4]*. Instituto Geológico, Minero y Metalúrgico-INGEMMET. Retrieved from https://repositorio.ingemmet.gob.pe/handle/20.500.12544/114
Wimpenny, S., Copley, A., Benavente, C., & Aguirre, E. (2018). Extension and dynamics of the Andes inferred from the 2016 Parina (Huarichancara) Earthquake. *Journal of Geophysical Research: Solid Earth*, *123*, 8198–8228. https://doi.org/10.1029/2018JB015588
Wolfe, F. D., Stahl, T. A., Villamor, P., & Lukovic, B. (2019). Short communication: A semi-automated method for rapid fault slip analysis from topographic scarp profiles. *Earth Surface Dynamics*, 1–17. https://doi.org/10.5194/esurf-2019-53
Zaro, G., Nystrom, K. C., & Keefer, D. K. (2013). Environmental catastrophe and the archaeological record: Complexities of volcanism, floods, and farming in South Coastal Peru, AD 1200-1700. *Andean Past*, *11*(1), 17.
Zwick, P., McCaffrey, R., & Abers, G. (1994). *MT5 Program* (Vol. 4). IASPEI Software Library.